FRACTURE AND DEFORMATION OF LiF BICRYSTALS UNDER IMPACT EROSION AND QUASI-STATIC INDENTATION

by

Jong Yeon Lee

A DISSERTATION

Submitted to

Michigan State University

in partial fulfillment of the requirements

for the degree of

DOCTOR OF PHILOSOPHY

Department of Metallurgy, Mechanics, and Materials Science

1985

ABSTRACT

FRACTURE AND DEFORMATION OF LiF BICRYSTALS
UNDER IMPACT EROSION AND QUASI-STATIC INDENTATION

by

JONG YEON LEE

LiF bicrystals were eroded by particle impact so as to understand the role of grain boundary on fracture and deformation during impact erosion. LiF bicrystals with grain boundaries possessing only tilt character were eroded with blunt 0.5 mm quartz sand particles under normal impact at room temperature. The damage patterns produced by impact of particles whose velocities ranged from 2.5 to 20 ms^{-1} were studied by optical and scanning electron microscopy.

Experimental results of crack propagation caused by particle impact are discussed and compared with the predictions by a model of mode I crack propagation based on the normal stress law for brittle fracture. Such an analysis implies that the crack propagation direction in crystals with strong cleavage tendencies is mainly governed by the anisotropy of surface energy, regardless of the method of the crack initiation. The mechanism of material removal in LiF bicrystals under particle impact is the interaction of lateral fractures with other lateral fractures or grain boundaries. Fine slip occurs as a result of particle impact, and such fine slip is usually blocked by the tilt boundary. Slip propagation through the grain boundary was rarely observed under such conditions.

Damage caused by quasi-static indentation is compared with that due

to particle impact. Lateral fractures are not produced by quasi-static indentation of the LiF bicrystals. Indentation loading produces wide slip bands whose interaction with tilt boundary results in propagation of slip through the boundary. The main factors influencing the slip propagation through tilt boundaries under indentation loading are the indentation distance from the grain boundary, relative crystallographic orientation, and the magnitude of indentation load. The critical indentation distance for slip propagation decreases as the misorientation angle increases. In a semi-brittle material like LiF, deformation and fracture caused by quasi-static indentation are not representative of damage resulting from particle impact.

ACKNOWLEDGEMENTS

The author wishes to express his deepest appreciation to his advisor, Dr. Karatholuvu N. Subramanian, for his guidance and help during the course of this study. He sincerely thanks also to his graduate committee, Dr. R. Summitt, Dr. N. Altiero, Dr. C. Foiles, and Dr. P. Schroeder, for their review and discussion. The entire faculty and staff of the Department of Metallurgy, Mechanics, and Materials Science are thanked for their assistance and helpful discussion.

He is grateful to his fellow graduate students for their help and friendship.

Finally, to his wife and two sons, the author expresses his deep gratitude for their patience and encouragement.

TABLE OF CONTENTS

LIST OF TABLES

LIST OF FIGURES

Page

I. INTRODUCTION

Mechanical damage introduced in materials by the impact of small particles is of considerable academic and practical importance. Materials can be eroded by the abrasive actions of solid particles present in flowing liquids or compressed gases. Such erosion by particle impact is a very common and important phenomenon since it can cause significant material loss and mechanical degradation of the material.

There are many examples illustrating the significance of erosion by particle impact in engineering practice. Performance restrictions on the useful life of gas turbine blades, coal conversion plants, rocket nozzles, and helicopters operating in sandy region are based on such erosion. On the other hand, the destructive aspects of the erosion process are utilized in drilling, rock cutting, and sand blasting operations.

Erosion of materials by particle impact is a complex process involving fracture nucleation, growth, and interaction which leads to removal of material from the exposed surface. Such complex erosion behavior is affected by various factors such as fluid pressure, temperature, particle velocity, particle shape and hardness, impingement angle, and surface conditions and micro-structure of the target material. There have been several investigations dealing with such environmental factors[1-15]. However, most of those investigations have dealt with macroscopic erosion behaviors of amorphous materials or fairly complicated industrial materials containing a large number of grains and

multiple phases.[8-15] As a result, obtaining a basic understanding of the mechanism of erosion under particle impact has been difficult. Studies on simple model systems are essential to obtain a basic understanding of erosion mechanism.

1.1 Material Selection

A simple model material is desirable for the investigation of fundamental mechanisms of erosion by particle impact. A target material which has well-defined slip systems and cleavage planes, and exhibits both elastic and limited plastic contact behavior (semi-brittle) would be appropriate for such a study concerned with microscopic aspects of impact erosion. LiF bicrystal is an ideal model system for such studies, since it will satisfy all of the above requirements. In addition, LiF bicrystal possess only one grain boundary.

Some of the other advantages in using LiF for the present study are the following: LiF is moderately plastic at room temperature and very resistant to atmospheric corrosion. Grain boundaries and slip lines can be observed clearly using etch pit techniques. Due to its low solubility in water, the damage introduced by the particle impact can be preserved during washing and etching process. Its optical transparency is also helpful in determining the extent of damage caused by particle impact by conventional optical microscopy.

1.2 Crystallography of LiF

Lithium fluoride is a transparent ionic crystal possessing rock-salt structure which is actually an fcc lattice with a cation and an anion as a basis.[16] This structure is a nearly perfect example of ionic bonding with alternate lattice sites occupied by cations (Li^+) and anions (F^-) as

shown in figure 1. The unit cell is composed of two interpenetrating face centered cubic structures, one of Li^+ ions and one of F^- ions, displaced relative to each other by a distance of half the lattice parameter along one of the three <100> directions.

The slip systems in LiF are simple ones. The primary slip planes are the {110} type planes and the secondary slip planes are the {001} type. The slip directions are $<1\bar{1}0>$ in both cases. There is only one $<1\bar{1}0>$ direction in each {110} slip plane. The projection of the six {110} planes onto the (001) plane is shown in figure 2. There is only one kind of mobile dislocation in each active slip plane and hence the complication of dislocations with different Burgers vectors to be found in the same slip plane can be avoided. Since no two primary slip planes have the same slip direction, cross-slip at room temperature is improbable. At room temperature, the primary cleavage planes are {001} type planes and the secondary cleavage planes are {110} type planes.

1.3 Objectives of This Research

The main objective of this study is to gain a better understanding of the basic mechanism of erosion by particle impact. For this study, the roles of microscopic deformation and fracture on erosion mechanism are investigated experimentally by analyzing the mechanisms of the slip propagation and material removal. The mechanisms of crack initiation and propagation are also analyzed by comparing the experimental results with the predictions of a model for mode I crack propagation based on normal stress law for brittle fracture. Besides, the roles of relative crystallographic orientation, grain boundary orientation, and particle velocity is investigated experimentally since they affect the erosion behavior of LiF bicrystals. A study of the damage introduced by quasi-static

Figure 1. Crystal structure of lithium fluoride.

Figure 2. Projection of {110} slip planes onto (001) surface of LiF crystal (Ref. 17).

5(a)

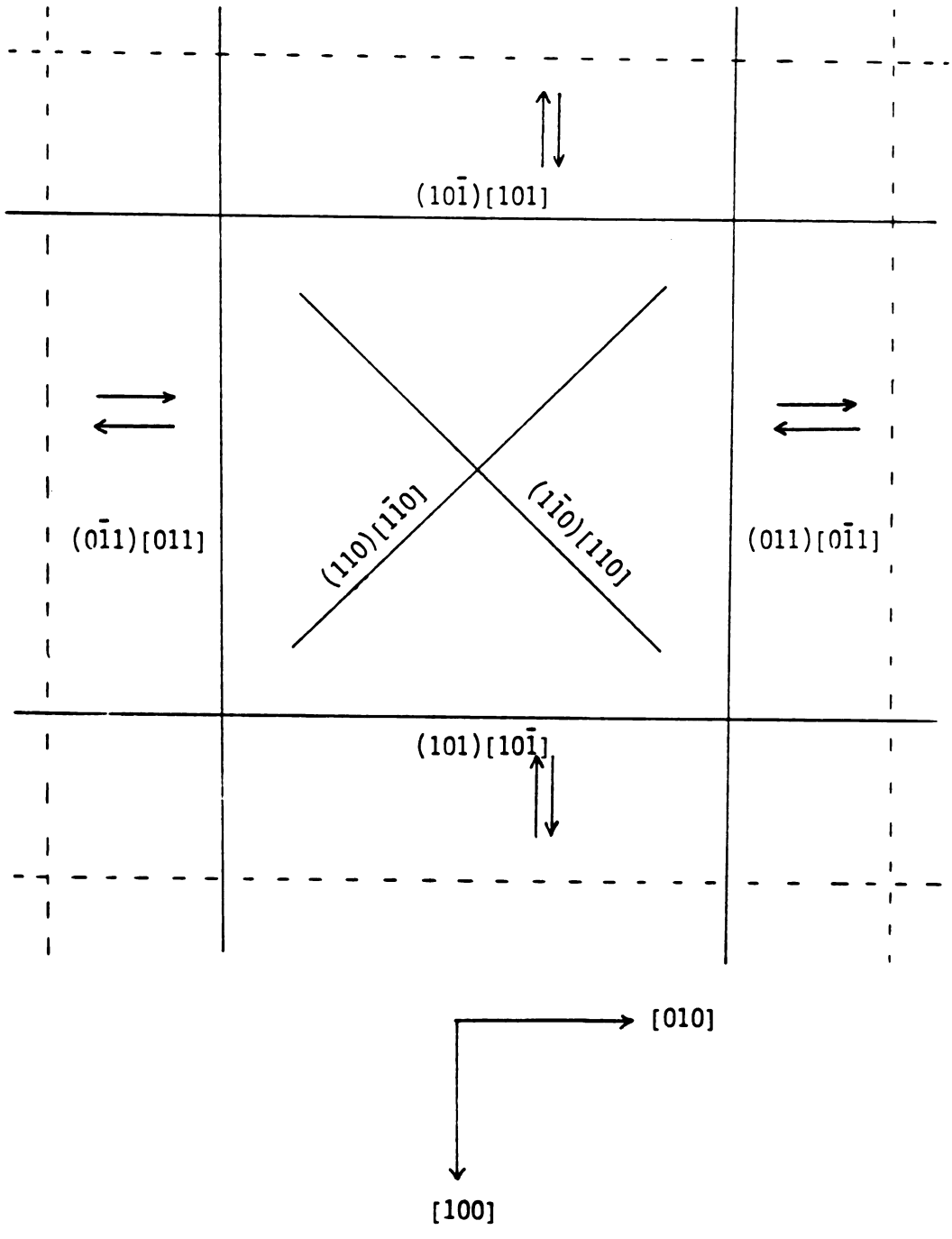
(10$\bar{1}$)[101]
(0$\bar{1}$1)[011]
(110)[1$\bar{1}$0]
(1$\bar{1}$0)[110]
(011)[0$\bar{1}$1]
(101)[10$\bar{1}$]
[010]
[100]

indentation is also carried out in order to investigate the slip propagation conditions in LiF bicrystals. By comparing the damage produced by particle impact with that produced by indentation, the effect of loading rate on the deformation and fracture is discussed.

II. THEORETICAL STUDIES AND HISTORICAL BACKGROUND

2.1 Fracture and Deformation of Materials by Impact Erosion

When particles impact on the surface of material, they leave either plastic impressions or small chipped regions at the region of impact. The plastic impressions are formed when the stresses at the impact site do not exceed the threshold value for fracture. In the elastic region, the maximum tensile stresses are radial, and in the elastic/plastic region, the maximum tensile stresses are tangential. On the other hand, in the sub-surface, the maximum tensile stresses are approximately parallel to the surface.[18]

Considering the directions of the maximum tensile stresses introduced by particle impact, the radial cracks propagate from the contact zone on planes normal to the surface, and the lateral cracks propagate outward from the base of contact zone on planes nearly parallel to the surface. The radial cracks are the main source of strength degradation of the target material while the lateral cracks are responsible for material removal by particle impact.[19]

Most theories of erosion of brittle materials are based on Hertz's analysis of the stresses generated when an isotropic, linear elastic surface is subjected to normal loading by a smooth spherical projectile. The radius of circular elastic contact is given as[20]

$$a^3 = \frac{3}{4} KPR \quad , \tag{1}$$

where a is radius of the circular elastic contact,

P is applied normal load,

R is radius of spherical projectile,

$$K = \left(\frac{1-\nu_1^2}{E_1} + \frac{1-\nu_2^2}{E_2} \right) ,$$

ν_1 is Poisson's ratio of specimen,

ν_2 is Poisson's ratio of projectile,

E_1 is Young's modulus of specimen, and

E_2 is Young's modulus of projectile.

The distance of mutual approach (Z) between the specimen surface and the impacting particle is[20]

$$Z = \frac{a^2}{R} . \tag{2}$$

These two equations specify the loading conditions for particle impact.

The relationship between the applied normal load (P) and the velocity of projectile (V) can be obtained by equating the kinetic energy of the impacting particle to the strain energy at the time of maximum impression:

$$\frac{1}{2} mV^2 = \frac{1}{2} \left(\frac{4}{3} \pi\rho R^3\right)V^2 = \int_0^{Z_{max}} P(Z)dZ , \tag{3}$$

where m is mass of the projectile, and

ρ is density of the projectile.

According to the solution by Timoshenko and Goodier[21], the maximum contact load (P_m) is

$$P_m = 1.14 \left\{ \left[\frac{16}{9\pi^2} \right] \left[\frac{m^3 V^6 R}{(C_1 + C_2)^2} \right] \right\}^{\frac{1}{5}} , \tag{4}$$

where, $$C_1 = \frac{1-\nu_1^2}{\pi E_1} \quad ,$$

and

$$C_2 = \frac{1-\nu_2^2}{\pi E_2} \quad .$$

By relating equation (4) with the mass of the projectile and the projectile density,

$$P_m = 1.52\ R^2\ \left[\frac{\pi V^6 \rho^3}{(C_1 + C_2)^2}\right]^{\frac{1}{5}} \quad . \qquad (5)$$

Thus, the maximum normal load can be related to the impact velocity and radius of the particle:

$$P_m = CR^2V^{\frac{6}{5}} \quad , \qquad (6)$$

where C is a constant.

Rickerby et al[22] modelled the impact process by assuming that all of the kinetic energy of the particle is used in permanently deforming the target, i.e.

$$P_cV_c = \frac{1}{2}\,mV^2 \quad , \qquad (7)$$

where p_c is pressure over the contact area (dynamic hardness),

v_c is crater volume, and

V is the velocity of projectile.

This equation can be rewritten as

$$p = \frac{mV^2}{2\pi d^2 \left(R - \frac{d}{3}\right)} \quad , \tag{8}$$

Where d is crater depth. Thus, the crater depth can be calculated by this equation when the dynamic hardness value is known since other parameters can be obtained experimentally. The dynamic hardness is the resistance of a material to indentation under dynamic load, and can be defined by using the equation given by Tabor,[23]

$$H_d = \frac{\frac{1}{2} m\left(V_i^2 - \frac{3}{8} V_r^2\right)}{v_c} \quad , \tag{9}$$

where, H_d is dynamic hardness,

m is the mass of the projectile,

V_i is the incident velocity of projectile,

V_r is the rebound velocity of projectile, and

v_c is the volume of the indentation.

From equation (9), dynamic hardness can be determined experimentally by measuring the incident and rebound velocities of the projectile and the size of the residual indentation.[27]

The crucial contact parameters in determining the mode and the extent of the damage caused by particle impact are the pressure, the contact radius, and the contact time. The pressure determines whether the target response will be elastic or plastic, the contact radius relates the pressure to the effective applied force, and the contact time determines the force history. The pressure and contact radius can be changed by changing the size and material of projectiles, and

the projectile velocity.

According to the investigations of Evans and Wilshaw[18], the contact time of WC particles (400 μm diameter) on ZnS target was found to be 2.2 μsec at the velocity of 520 m/sec. From the results of impact erosion in Pyrex and soda-lime glasses impacted by small steel spheres (800-1000 μm), Knight et al [20] concluded that the reflected stress pulse does not play a crucial role in the initiation of impact damage as evidenced by the shorter contact time (≈1 μsec), which is far less than the time for the reflected wave to return to the contact zone (> 2 μ-sec). Length of the contact time measured by Knight et al is very similar to that obtained by Evans and Wilshaw.

Wiederhorn and Hockey[24] studied the effect of material parameters on the erosion resistance of brittle materials by using SiC particles as projectiles. The erosion rate of the brittle target materials was found to decrease as the toughness of the target material increases. At 500 and 1000^{o}C, the erosion rate of silicon and hot-pressed silicon nitride increased slightly, whereas the erosion rate of glass, saphire, and sintered aluminum oxide was reduced. By examining the morphology of eroded surfaces they observed that as the toughness of the material increased, the relative number of impacts that result in chipping is reduced regardless of impact velocity.

In addition to the contact parameters, the ductility of the target material is another important factor in determining the erosion mode. The ductile erosion mode, which is typical in most metallic targets, is characterized by maximum erosion occurring at an impact angle of about 30 degree.[25] On the other hand, in ceramics and glasses, the brittle erosion mode where maximum erosion occurs by normal impact is typical.

In brittle materials, Hoff et al [26] observed a critical velocity below which there is no erosion and above which ceramics and glasses fail rapidly due to severe crack propagation.

According to the investigations of Chaudhri et al[27], most of the energy of the impacting particle is dissipated in the plastic deformation of the target material. The energy loss can be classified as follows,

(i) the energy dissipated by the plastic flow of the target material (major loss),

(ii) the energy of the elastic waves generated by impact (less than 10%)[28],

(iii) surface energy of the cracks formed (less than 5%), and

(iv) kinetic energy of detached fragments (negligibly small).

Ashford[29] recorded a fivefold reduction in the strength of silicon carbide rods impacted by small steel spheres indicating that the mechanical damage associated with particle impact can be severe although the damage may be barely detectable by visual inspection. Wiederhorn and Lawn[30] studied the nature and extent of strength degradation in soda-lime glass by impacting with spheres of steel and tungsten carbide. Examination of the sections of impacted specimens revealed well-defined cone cracks at low impact velocities. The threshold velocity for cone formation was typically 10 to 20 ms^{-1}. At intermediate velocities median cracks were initiated, and when the projectile velocity was high (50 to 100 ms^{-1}), the median cracks provided the main source of degradation since they extend deeper into the specimen. Also, at this stage, rapid unloading caused the Hertzian cracks to bend back abruptly towards the surface.

Knight et al [20] studied impact erosion in Pyrex and soda-lime glasses impacted by small steel spheres. In Pyrex glass, well developed cone cracks were observed outside the contact zone with semi-apex angle of ~50° at the crack velocities of 1400 to 1500 ms^{-1}. These cone cracks turned up toward the surface during the unloading procedure. In soda-lime glass, a large number of fine splinter cracks were initiated beneath the impact site and propagated along the trajectories of maximum tensile stress. Fracturing beneath the impact site was found to be completed within 4 to 5 micro-seconds, and the maximum magnitude of the cone crack angle was 63° in Pyrex glass. The impact damage observed by Evans and Wilshaw[18] under fully plastic contact conditions in ZnS has been shown to be identical in form to that obtained by indentation, consisting of radial, lateral and median cracks outside a plastic contact zone.

2.2 Fracture and Deformation of Materials by Indentation

The indentation test is probably the simplest method for obtaining a measure of the strength of materials. It has two unique advantages: (i) it can be applied to very small specimens which are in the general form during development of materials on a laboratory scale, and (ii) it is capable of measuring the fracture toughness of a material of small size not suitable for conventional fracture toughness testing.[31] The major disadvantage of this method is the detrimental effects of residual stresses associated with the indentation on the over-all properties of finished material.

The indentation is usually made by slowly pressing the indenter into the solid and maintaining the load for several seconds. The representative strain rate is of the order 5×10^{-2}/sec.[27] Stress and strain distributions due to several types of indentations in isotropic

continuous medium have been analyzed by using the continuum theory. Those results can not be applied directly to single crystals having well-defined slip systems and cleavage planes due to their anisotropic character. This situation is also true when the size of the projectile is smaller than individual grains in a polycrystalline solid.

In order to establish the nature of the indentation damage and indentation stress field, it is necessary to specify the parameters such as contact geometry, loading conditions, temperature; and mechanical properties of the specimen in details as evidenced by the results obtained by several investigators.[32-40]

The shape of the indenter is an important factor in determining the nature of contact geometry and the stress field. Indenters are classified into two types: "blunt" indenters (shperes), characterized by the formation of a Hertzian cone crack; and "sharp" indenters (pyramids, cones), with a plastic contact resulting in the formation of median and lateral cracks. When a pyramid indenter is used, the contact pressure is independent of indent size, and thus a pyramid indenter is ideal for indentation test.[41]

A Boussinesq stress field is developed when an isotropic, linear elastic half-space is subjected to normal loading by a sharp indenter such as pyramid indenter used in the Vickers hardness test. From the contact geometry, the mean contact pressure can be expressed as

$$P_o = \frac{P}{C\pi a^2} \quad , \tag{10}$$

where P_o is mean contact pressure,

P is applied load

C is constant depending on the geometry of indenter (C = 1 for symmetric indenter), and

a is radius of contact area.

The Boussinesq stress field due to sharp indenter can be written as follows in the curvilinear coordinate system shown in figure 3:

$$\sigma_{ij} = \left(\frac{P}{\pi R^2} \right) [f_{ij}(\phi)]_{\nu} \quad , \tag{11}$$

where P is applied load

R is radial distance from the point of contact, and

f_{ij} is independent angular function.

In this coordinate system, the stress components can be written as[42]

$$\sigma_{rr} = \frac{P}{\pi R^2} \left[\left\{ \left(\frac{1-2\nu}{4} \right) \sec^2 \frac{\phi}{2} - \frac{3}{2} \cos\phi \sin^2\phi \right] \right. \quad , \tag{12}$$

$$\sigma_{\theta\theta} = \frac{P}{\pi R^2} \left[\left(\frac{1-2\nu}{2} \right) \left(\cos\phi - \frac{1}{2} \sec^2 \frac{\phi}{2} \right) \right] \quad , \tag{13}$$

$$\sigma_{zz} = \frac{P}{\pi R^2} \left(-\frac{3}{2} \cos^3 \phi \right) \quad , \tag{14}$$

$$\sigma_{rz} = \frac{P}{\pi R^2} \left(-\frac{3}{2} \cos^2\phi \quad \sin \phi \right) \text{, and} \tag{15}$$

$$\sigma_{rz} = \sigma_{\theta z} = 0 \quad . \tag{16}$$

Figure 3. Co-ordinate system for indentation stress field.

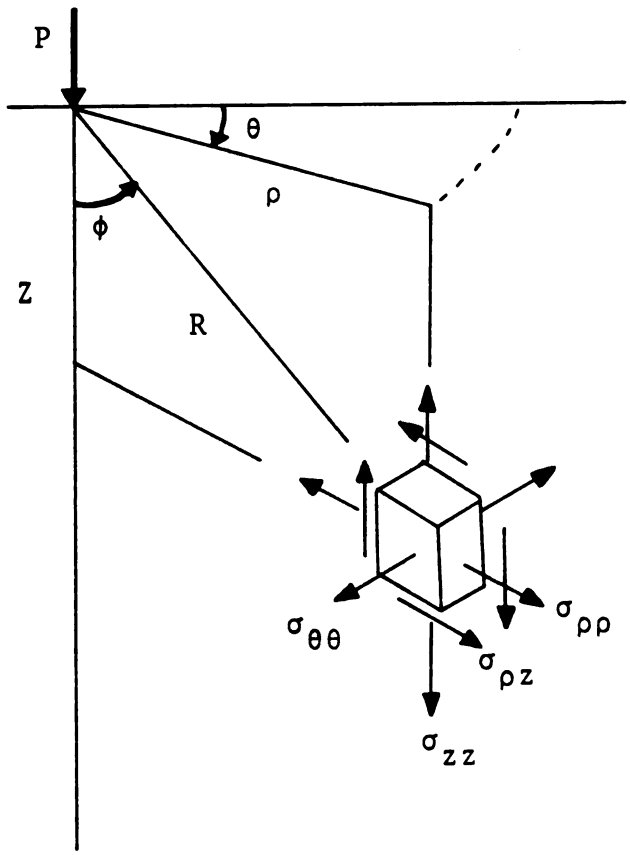
P
θ
ρ
ϕ
Z
R
σθθ
σρz
σρρ
σzz

The high stress concentration in the Boussinesq stress field can be relieved by non-linear and inelastic deformation, and the stress field becomes complicated due to the inelastic deformation. The stress field through which the cracks must ultimately propagate is relatively ill-defined, and tends to result in a more complex fracture pattern than in the Hertzian stress field caused by spherical indenter.[41]

Hagan and Swain[43] suggested that the deformation flow lines in the subsurface region are responsible for the median, radial, and lateral cracks that develop around indentations and ultimately lead to strength degradation of brittle materials. The formation of the median cracks to accommodate strains at the intersection of flow lines is just like crack nucleation from dislocations on two intersecting slip planes.[44, 45] However, the lateral cracks are initiated at nuclei at the elastic/plastic boundary or along the flow lines, and they are propagated by the unloading residual stresses.

Lawn and Evans[46] have obtained critical conditions for the initiation of the sub-surface flaws by indentation. The minimum load (P_c) to propagate the critical flaws is

$$P_c = 2.2 \times 10^4 \left(\frac{K_{IC}}{H} \right)^3 K_{IC} \qquad (17)$$

where K_{IC} is critical stress intensity factor and H is hardness. The size of the corresponding critical flaw (C_{min}) is given by

$$C_{min} = 44.2 \left(\frac{K_{IC}}{H} \right)^2 . \qquad (18)$$

By indentation of carbides with a Vickers indenter, Palmqvist[41] found that the load increased linearly with the crack length. By extending

Palmqvist's method, Dawihl and Altmeyer[48] noticed that the dependence of the crack length on the load was influenced by the character of the surface, and eliminated this problem by carefully polishing the specimen surface. Lawn et al.[41, 42, 49] established indentation as a technique for the determination of the toughness of brittle materials by investigating the indentation fracture. Lawn and Fuller carried out indentation tests on soda-lime glass and discovered that crack length increased with load P as $P^{2/3}$.[49] Crack length was observed to depend on the profile of the indenter as well as on the friction coefficient between the specimen and indenter. Evans[50] observed radial cracks in Si_3N_4 under pyramid indentation, but they were not observed in relatively coarse grained materials ($\gtrsim$20 μm grain size).

Petrovic and Mendiratta[51] investigated indentation - produced cracks in hot-pressed silicon nitride by using diamond pyramid and Knoop indenters. On the specimen surface, sharp cracks radiated from the corners of the diamond pyramid indentation, while for the Knoop indentation a sharp crack was observed along the long diagonal only under 25.5 N load. These cracks correspond to the "median vents" described by Lawn et al[41]

By 50 N load indentation in fused silica glass, Hagan[52] observed median and lateral cracks around the impression in sectioned specimen. He found that the dominant cracks in fused silica are cone cracks which do not form in soda-lime glass of similar surface finish. Median cracks were produced by the expansion of the compacted zone boundary beneath the indentation, while the mismatch of strain at this boundary lead to lateral crack formation during unloading.[52]

2.3 Single Crystal Studies

2.3.1 Impact erosion of single crystals

Some investigators[53-57] have studied the erosion behavior of single crystals by particle impact in order to gain a better understanding of the fundamental mechanism of erosion since single crystals are ideal models due to their well-defined crystal structure. Although the impact damage superficially resembles a Hertzian type fracture, the lateral fractures do not completely follow the path predicted by the Hertzian stress field; some compromise between the tendency for cracks to follow stress trajectories and cleavage planes occurs in single crystals.

Rickerby et al [22] studied the influence of particle properties on impact damage on mechanically polished {100} surfaces of LiF single crystals by using steel and WC spheres at velocities ranging from 50 to 350 m sec^{-1}. The typical damage which was observed by SEM consisted of a central crater formed by a combination of {110} $\langle 1\bar{1}0 \rangle$ slip and modes II and III cleavage crack propagation, and a surrounding region from which material loss occurred through intersection of {100} and {110} cleavage cracks.[22]

Single crystals of NaCl, MgO and LiF were deformed by impacting with glass and WC particles of diameter in the range of 0.4 - 1.0 mm, and their deformation and fracture behavior was analyzed by Chaudhri et al.[27] The dynamic hardness of these materials were determined and found to be several times the quasi-static hardness. At high strain rates the crystals were observed to behave in a brittle manner and the dynamic hardness increased linearly as the strain rates increased.

The dislocation rosette size around the impact sites also increased as the dynamic load increased. The material loss was found to occur both

during the loading and unloading parts of the impact.

Subramanian and Schuon[55, 57] investigated the microstructural aspects of impact erosion in single crystals of LiF, NaCl, KCl, and CaF_2 by using glass beads (0.25 mm diameter) and standard Ottawa quartz sand (0.5 mm diameter) as blunt projectiles. Some complete ring fractures were observed at the impact site and lateral fractures spreaded out from the contact zone. In NaCl and KCl, fractures on the (010) planes were found to develop as a result of dislocation reaction:

$$(\tfrac{a}{2})[011]_{(01\bar{1})} + (\tfrac{a}{2})[01\bar{1}]_{(011)} \rightarrow a[010]_{(010)} \ . \qquad (19)$$

In LiF, lateral fractures were formed through the dislocation reaction

$$(\tfrac{a}{2})[10\bar{1}]_{(101)} + (\tfrac{a}{2})[0\bar{1}1]_{(011)} \rightarrow (\tfrac{a}{2})[1\bar{1}0]_{(112)} \ . \qquad (20)$$

At 200 and 400°C, deformation was accommodated more easily in LiF crystal since secondary slip system {100}<011> also became active. Lateral fractures were not observed in specimens eroded at 400°C.

At normal impact, the length of the lateral fractures was found to be proportional to the diameter of contact zone. In LiF, the observed values of contact zone size were larger than the calculated values according to Hertz's analysis by a factor of about 10. This difference was attributed to the fact that plastic deformation is neglected in Hertz's analysis.[57]

The critical velocity was found to be much lower in CaF_2 than in more ductile materials such as LiF, NaCl, and KCl indicating that the critical velocity increases as the ductility of the material increases.

Micromachining was found to be a dominant mode of erosion in oblique impact as proposed by Finnie[58] when the impact angle is greater than 30^{o} from the normal to the surface in LiF, NaCl, and KCl.

2.3.2 Indentation of Single Crystals

In order to establish the nature of the stress field introduced by indentation, the mechanical anisotropy of the material is a critical factor to be considered. For the investigations on the effect of anisotropy of specimens during indentation, single crystals are ideal models because they exhibit strong anisotropic character due to their crystallographic nature. Some attempts have been made to study the deformation mechanism associated with indentation in single crystals.[60, 61]

By pyramid indentation of NaCl single crystal, Aerts et al.[59] found that the hardness depended somewhat on the orientation of the diagonals of the indentation figures with respect to the crystallographic axes of the lattice. Higher hardness values were obtained when one diagonal of the indenter was parallel to [100] as compared to a situation when it was parallel to [110]. This variation is attributed to the alteration in shape of the indentation figure as a result of the crystallographic anisotropy.[60] By using the dislocation etch pit technique, Vaughan and Davisson[61] studied dislocation behavior in LiF single crystals by indenting on (001) planes. They observed that the dislocation patterns consisted of edge dislocations extended along the <110> directions, and those of screw dislocations extended along the <100> directions. The insertion of the indenter into a (001) plane of LiF displaces planes of material along the <110> slip directions forming two rows of edge dislocations as shown in figure 4(A).[61]

Keh[60] studied dislocation rosette patterns produced by pyramidal and

Figure 4. (A). Displacement of material in the <110> directions forming rows of edge dislocations by indentation on the (001) surface of LiF crystal (Ref. 60).

(B). Dislocation pattern for a indentation on the (001) surface of MgO crystal (Ref. 60).

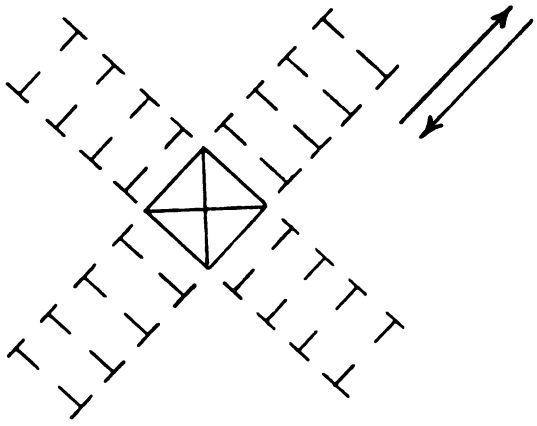

(A)

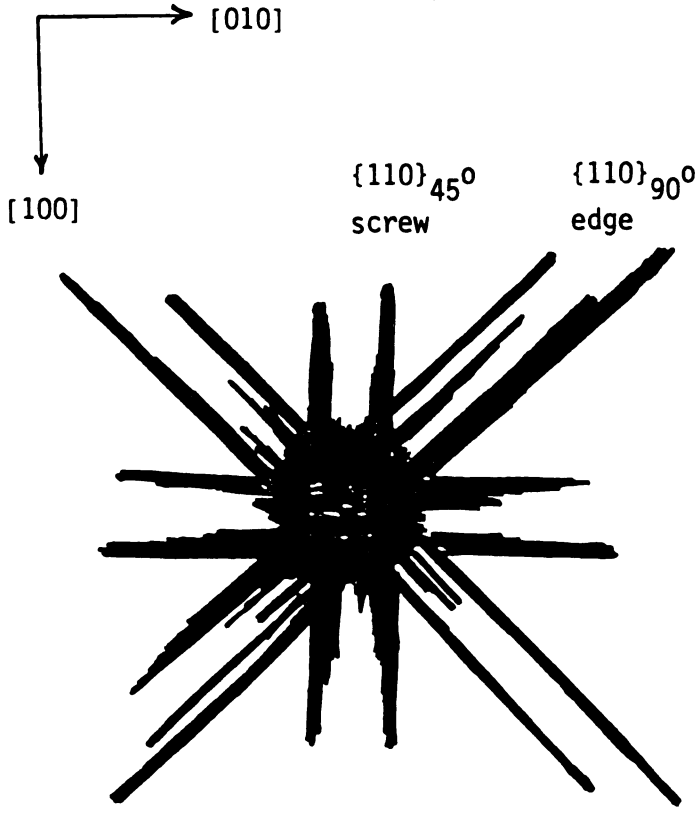

(B)

spherical indenters on the cleaved surfaces of MgO single crystals, which also have rock-salt structure. Etch pit studies of two-dimensional and three-dimensional dislocation structures, as shown in figure 4(B) and 5, revealed that all dislocation lines formed by indentation lie in the {110} primary slip planes. Two of the slip planes are perpendicular to (001) plane and can be referred to as $\{110\}_{90^o}$ planes. Four other slip planes are inclined at 45^o to the (001) plane and can be referred to as $\{110\}_{45^o}$ planes. From the crystal structure of MgO and etch pit patterns, the dislocation loops formed on the {110} type planes by indentation on (001) planes can be sketched as shown in figure 6. In this figure the etch pits in the <110> directions correspond to edge components since the dislocation segments are perpendicular to the Burgers vector. Those in the <100> direction are screw components because the dislocation segments are parallel to the Burgers vector. By measuring the distances (D) of travel of leading dislocations of the edge (e) and screw (s) dislocations on the $\{110\}_{45^o}$ and $\{110\}_{90^o}$ planes, the following relations were found by Keh.[60]

$$D_s \{110\}_{45^o} \cong 1.4\, D_e \{110\}_{90^o} , \tag{21}$$

$$D_s \{110\}_{45^o} \cong D_e \{110\}_{45^o} , \text{ and} \tag{22}$$

$$D_e \{110\}_{90^o} \cong 2D_s \{110\}_{90^o} . \tag{23}$$

During the process of indentation the material is pushed away from the indenter and dislocations are formed along the slip planes. Thus, the dislocations formed on the two sides of each wing are of opposite sign as shown in figure 5. Keh[60] observed that the dislocations with the same sign as the applied shear stress moved out along their slip planes.

Figure 5. Arrangement of edge dislocations on
(A). indented, and
(B). cleaved surfaces
of MgO crystal (Ref. 60).

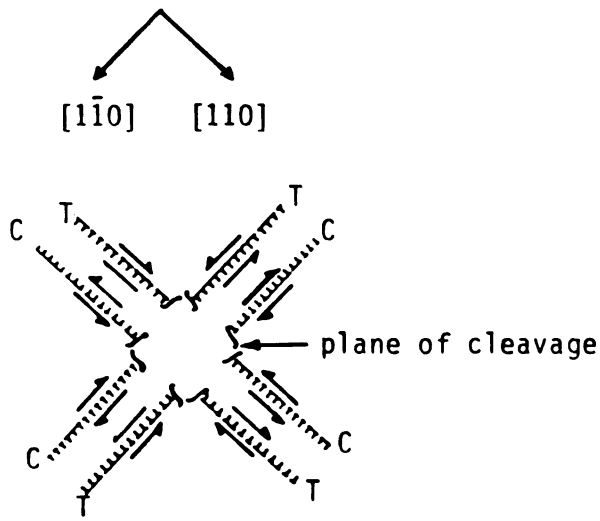

(A)

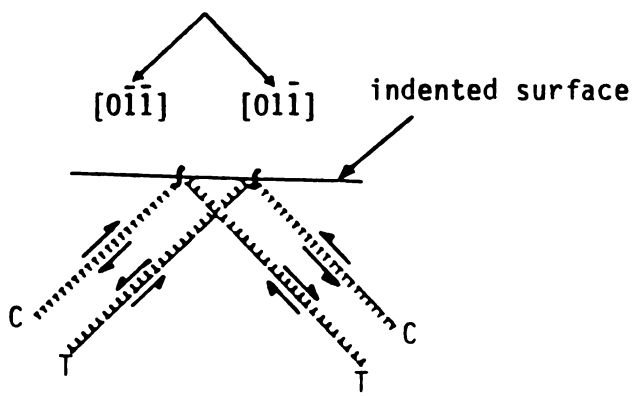

(B)

C:compression

T:tension

Figure 6. Slip planes and dislocation half-loops in indented MgO crystal (Ref. 60).

(A). $\{110\}_{45^o}$ planes: (101), (10$\bar{1}$), (0$\bar{1}$1), (011)

(B). $\{110\}_{90^o}$ planes: (110), (1$\bar{1}$0)

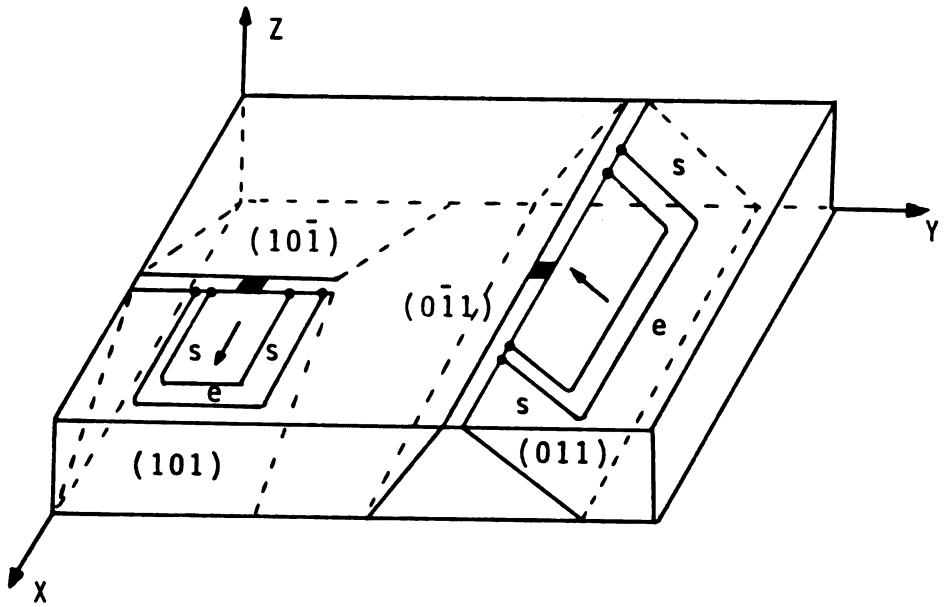

(A)

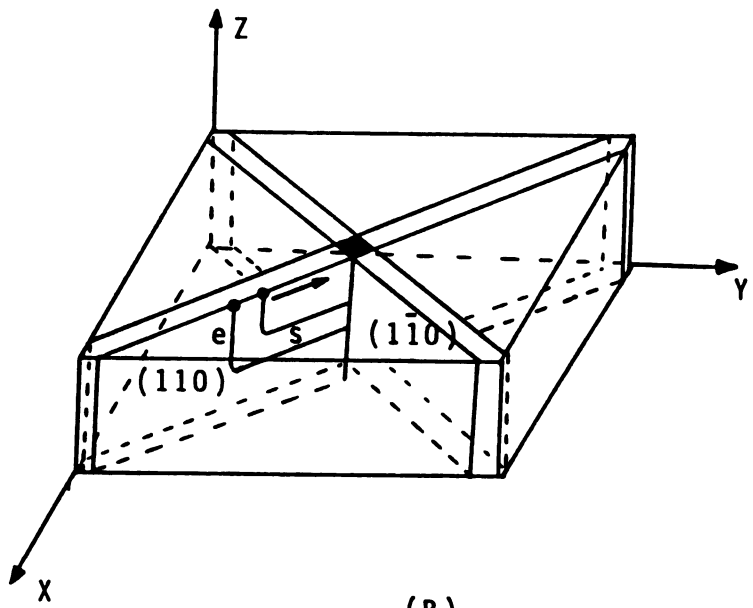

(B)

e : edge component

s : screw component

Johnston found that in MgO the linear velocity of the edge component of a dislocation half-loop is approximately 200 times that of a screw component of another loop under the same applied shear stress in a homogeneous stress field.[60] However, by the indentation method, Keh[60] observed that the distance of travel of the edge component of the leading dislocation is approximately the same as that of the screw component indicating that the stress field around an indentation is not homogeneous. Pyramid indentation on a cleaved (001) surface of a MgO crystal with small loads of a few grams caused cracking in the <110> directions.[60] With high indentation loads about 5 N and above, irregular cracking was observed. Chemical polishing revealed that these cracks were lying along the <110> direction and were present in the $\{100\}_{90}$° planes.

By indenting LiF single crystals at an indenter load of 10 N, Hagan[62] observed shear cracks in the subsurface region. These shear cracks are formed by the interaction of dislocations on intersecting $(110)_{90}$° and $(101)_{45}$° planes. Armstrong and Wu[63] also studied plastic deformation zones surrounding pyramid indentation in MgO single crystals. The total plastic deformation seems to be accounted for by slip on the six $\{110\}\ \langle 1\bar{1}0\rangle$ slip systems as shown in the figure 7. It was proposed that the edge dislocations on adjacent slip systems interact and generate a sessile dislocation which forms a nucleus for cracking on the $(\bar{1}10)$ plane.[63]

$$(\tfrac{a}{2})[10\bar{1}]_{(101)} + (\tfrac{a}{2})[0\bar{1}1]_{(011)} \rightarrow (\tfrac{a}{2})[1\bar{1}0]_{(112)} \quad . \tag{24}$$

The reacted $(\frac{a}{2})[1\bar{1}0]$ edge dislocation with its line vector parallel to $(\frac{1}{\sqrt{3}})[11\bar{1}]$ is sessile because it is contained in the (112) plane which is not a slip plane in MgO. According to their observation, four $\{\bar{1}10\}$ cracks spread outward from indentations on the (001) cleavage plane of MgO

Figure 7. Schematic drawing of indentation damage on (001) surface of MgO crystal involving {101} <101> slip and <110> surface cracking (Ref. 63).

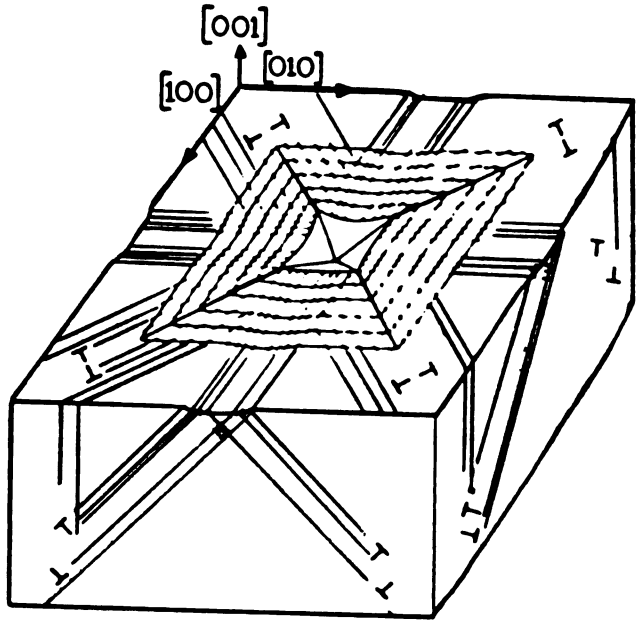
[001]
[010]
[100]

at 1 to 5 N load at room temperature.

2.4 Role of Grain Boundaries on Fracture and Deformation of Materials

Grain boundaries are the most important barrier to dislocation motion during the early stages of plastic deformation of polycrystalline solids. The influence of grain boundaries on the mechanical properties of materials has long been recognized, and various theories and models have been proposed for the structure of the boundary region between adjacent crystals.

Dislocations pile-up on slip planes at grain boundaries during plastic deformation. When the pile-up contains many dislocations, stress concentration of the order of the threshold shear stress can develop. However, because of the difficulties in forcing a dislocation from one grain into another, it is to be expected that slip will spread from one grain into its neighbor by the process of introducing sources of dislocations in the adjacent grain to become active.[64]

When the slip planes on either side of the grain boundary are almost coplanar (small misorientation), the shear stress concentration ahead of the dislocation pile-up results in slip propagation into the adjacent grain and relaxes the stress concentration without forming cracks. According to the investigations of Johnston et al[65] with MgO bicrystals under compression, when a single slip band impinged upon the small tilt boundary ($0\text{-}5^{o}$), both edge and screw type slip bands propagated across the boundary without crack nucleation.

Sadananda and Marcinkowski[66] analyzed the deformation of grain boundaries geometrically by using the slip systems as reference coordinate axes to describe the orientation of the two grains. As pointed

out Lange[67], for a complete mathematical description of a boundary separating two crystals, five parameters are necessary since such a boundary has five degrees of freedom. Figure 8 shows how the grain coundary is specified with respect to the two slip systems in adjacent grains. $\underline{b}_1$ and $\underline{b}_2$ are the Burgers vectors and $\underline{n}_1$ and $\underline{n}_2$ are vectors normal to the slip plane in grain I and II respectively. $\underline{n}_I$ is the outward normal to the boundary before deformation. The relation between the two systems of coordinates is shown in figure 8(B). As illustrated in figure 9, for the passage of a dislocation from grain I to grain II, the magnitude of the Burgers vector and the interplanar distances need not be the same in both the grains.[66]

The continuity of slip planes across the grain boundary is established by the presence of boundary dislocations.[66] A disturbance is left at the boundary when a dislocation passes from one grain to the other due to the misorientation and the difference in magnitudes of the slip vectors. Such a disturbance is characterized by an effective Burgers vector ($\underline{b}_I$) given by

$$\underline{b}_I = (\underline{b}_1 - a\underline{b}_2) \quad , \tag{25}$$

where 'a' is the directional cosine between primed and unprimed co-ordinates axes as shown in figure 8(B).[66] As a result of shear, the boundary itself undergoes shape and orientation changes that can be determined from the geometrical properties of the dislocations responsible for the shear.[65]

Johnston et al [65] concluded that the probability of crack nucleation by dislocation pile-up increases with increasing misorientation across the grain boundary. They observed that edge bands($\{110\}_{90}o$)were

Figure 8. (A). Coordinate axes in two adjacent grains.
(B). Relationship between the two systems of coordinates (Ref. 66).

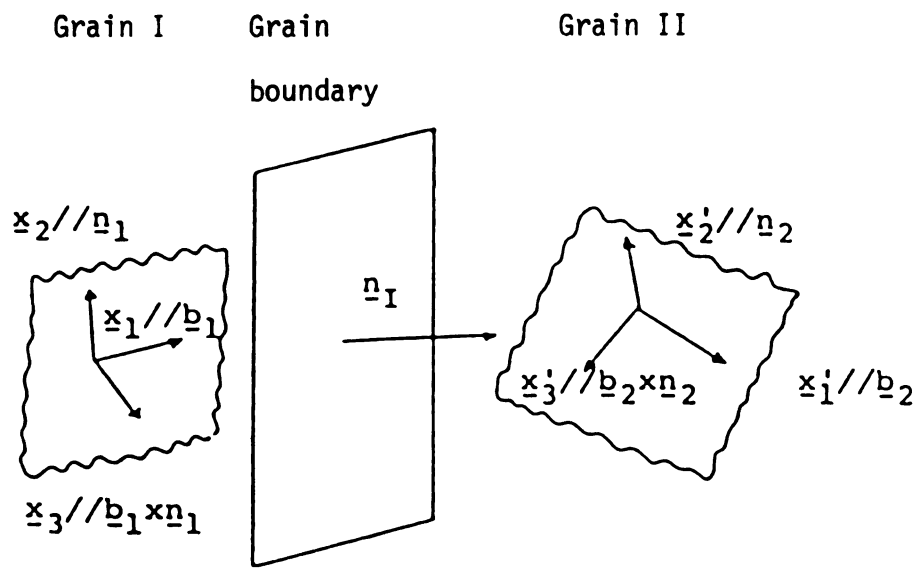
Grain I
Grain boundary
Grain II
$\underline{x}_2//\underline{n}_1$
$\underline{x}_1//\underline{b}_1$
$\underline{x}_3//\underline{b}_1 x \underline{n}_1$
$\underline{n}_I$
$\underline{x}_2'//\underline{n}_2$
$\underline{x}_3'//\underline{b}_2 x \underline{n}_2$
$\underline{x}_1'//\underline{b}_2$

(A)

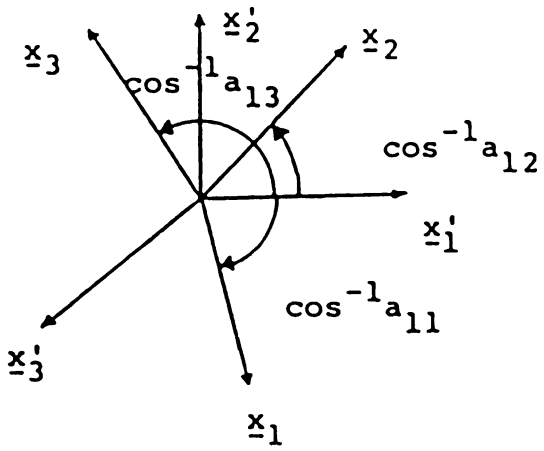
$\underline{x}_2'$
$\underline{x}_3$
$\underline{x}_2$
$\cos^{-1} a_{13}$
$\cos^{-1} a_{12}$
$\underline{x}_1'$
$\cos^{-1} a_{11}$
$\underline{x}_3'$
$\underline{x}_1$

(B)

Figure 9. Passage of a dislocation from one crystal into the other (Ref. 66).

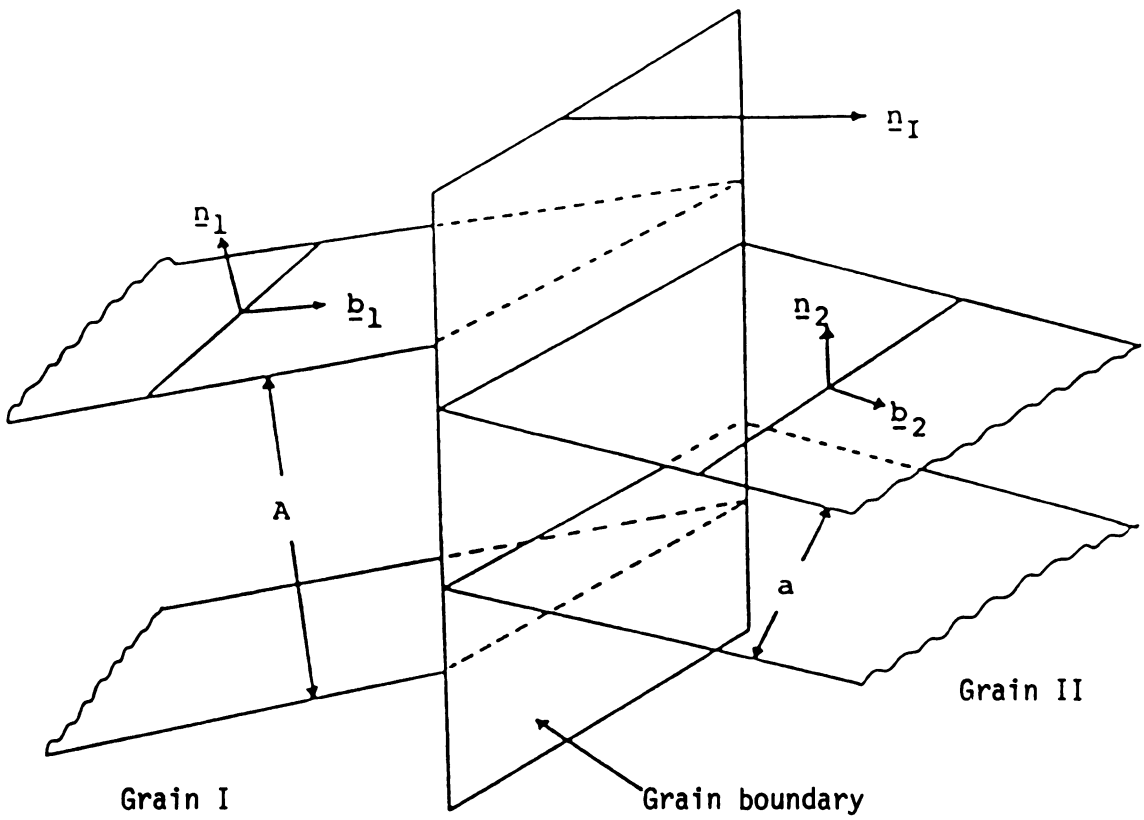

A: Magnitude of the Burgers vector

a: Interplanar distance

associated with transcrystalline cracks and screw bands($\{110\}_{45}^{o}$)either terminated at, or passed through, the boundary without forming cracks for a medium tilt plus medium twist boundary in MgO bicrystals.[65] For a large tilt plus large twist boundary, edge bands were associated with intercrystalline cracks according to the classical Zener model.

Westwood[68] proposed from the observations on MgO bicrystals that cracks may be nucleated at a low angle grain boundary only through the superposition of the tensile stress fields of two dislocation pile-ups generated on both sides of the boundary.

Carnahan et al [69] showed that in silver chloride, the mode of slip controls the role of grain boundaries on mechanical behavior. When plastic deformation occurs by pencil glide, grain boundary has only a minor effect on the flow stress. But, at temperatures where plastic deformation is confined essentially to planar slip, they exert a strong influence on the flow stress and fracture behavior. According to the studies by Johnston et al [70], KCl single crystal can be extended by as much as 40% at room temperature, while a KCl polycrystal fractures with very limited macroscopic deformation, indicating the strong influence of grain boundaries on deformation and fracture.

Lee and Subramanian[71] investigated the role of relative crystallographic orientation and grain boundary orientation relative to the crack front on crack propagation in LiF bicrystals. The anisotropy in surface energy governs the direction of crack propagation due to the strong cleavage tendency of LiF crystal. This was evidenced by the observations that the crack paths change at the grain boundary according to the crystallographic orientation of the adjacent grain, and grain boundary orientation relative to the crack front. In the specimens

having small misorientation angles, transcrystalline crack propagation along the primary cleavage planes was the dominant fracture mode. For specific relative crystallographic misorientation and grain boundary orientation, primary and secondary cleavage cracks were initiated simultaneously at the grain boundary resulting in crack branching. Intercrystalline fracture was also observed when the grain boundary orientation angle is smaller than the critical angle at which intercrystalline fracture and transcrystalline cleavage occur simultaneously. These results were consistent with a model based on surface energy considerations.

III. EXPERIMENTAL PROCEDURE

3.1 Bicrystal Growth and Specimen Preparation

Lithium fluoride single crystals were grown by Czochralski method (figure 10), using LiF single crystal seed. LiF melt was obtained by heating LiF powder obtained from Kawecki Chemical Company in a graphite crucible. The chemical composition of LiF stock is given in the table 1. Details of the Czochralski furnace used and the condition employed during crystal growth are the following: The heating element and crucible were made of high density graphite (AUC), and the furnace was water-cooled. Two chromel-alumel thermocouples were placed at diametrically opposite points, and a potential-divider circuit was used to find the average thermo-emf. Argon gas was used to provide an inert furnace atmosphere. The crucible and the seed were rotated in opposite directions at the rate of approximately one to two revolutions per minute to obtain a homogeneous melt and a planar solid-liquid interface. The crystals were grown at the rate of 6 to 12 mm per hour.

The single crystals were cleaved and used as seeds to grow LiF bicrystals by the Czochralski method. The procedures for growing the bicrystals by the Czochralski method were the same as those employed for growing single crystals. In order to grow bicrystals having simple tilt character, two seeds were held by two seed rods fixed parallel to each other as shown in figure 11. The relative crystallographic orientation of the two grains in the bicrystal was controlled by the setting of the two seeds.

Bicrystal specimens having single tilt character were cleaved by using chisel and hammer since (001) planes in both grains matched as a

Figure 10. Czochralski furnace used for growing LiF crystals.

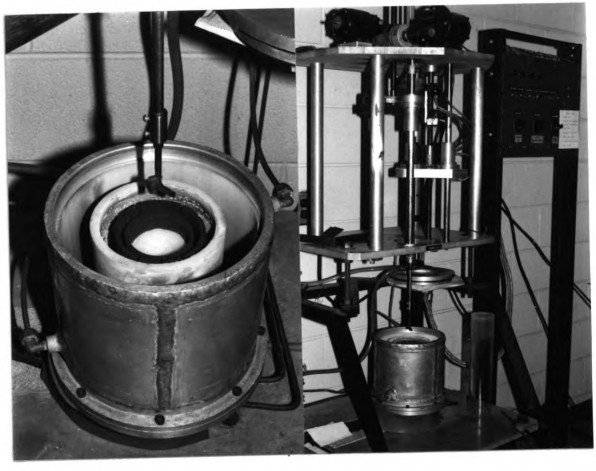

Table 1. Chemical composition of LiF powder

(weight percent)

LiF	99.200 %
H_2O	0.700 %
SO_4	0.050 %
Acidity as HF	< 0.040 %
Fe_2O_3	< 0.020 %
Na	< 0.005 %

Figure 11. Seed setting used for bicrystal growth.

(A). Schematic drawing.

(B). Top view.

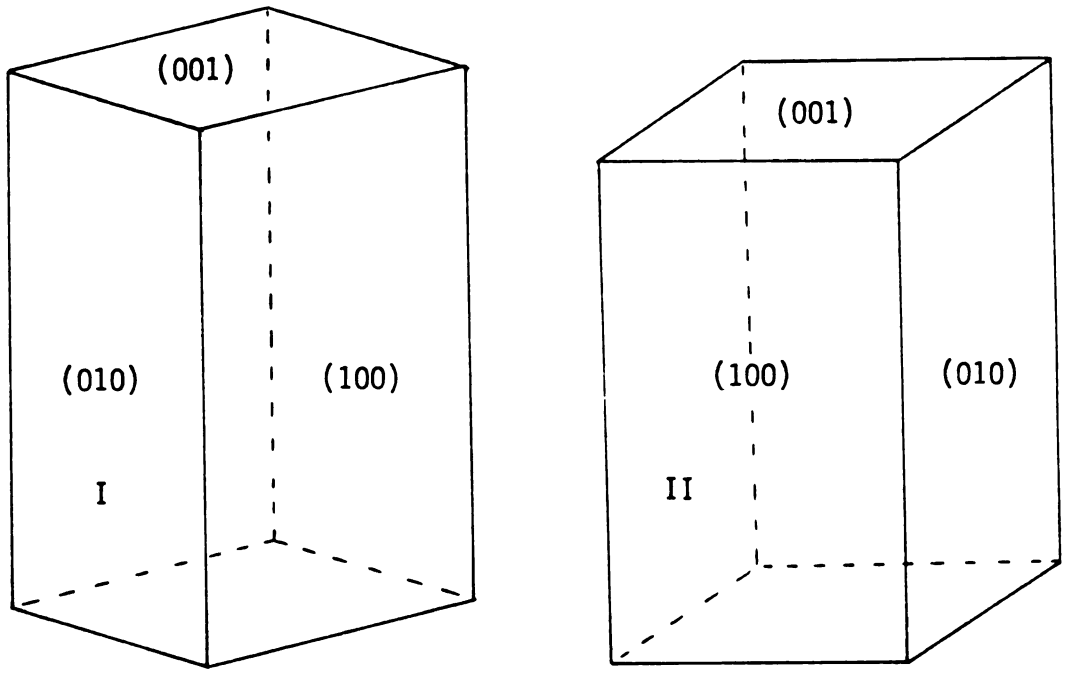

(A)

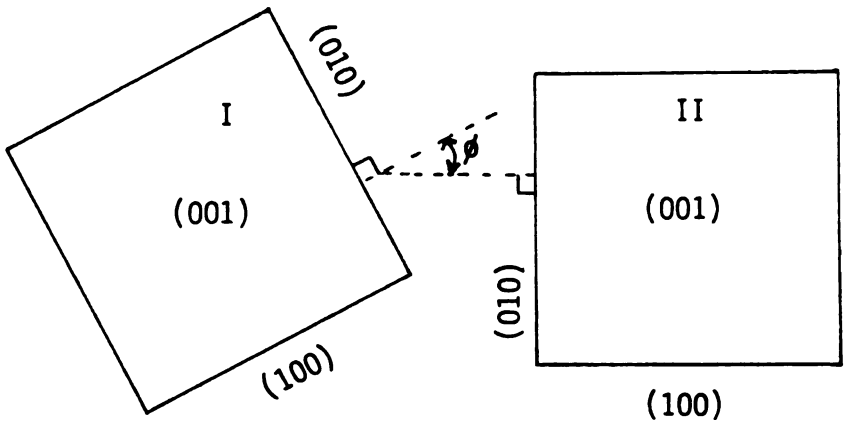

(B)

plane. The cleaved specimens were stored in a desiccator in order to minimize degradation from moisture and mechanical damages. The specimens used for the study were thin discs (3 mm thick, and 15 mm in diameter).

3.2 Impact Erosion Test

Standard Ottawa quartz sand was used as blunt projectiles. The surface of the projectile is highly weathered and rounded as shown in figure 12. To achieve a uniform particle size for the present investigation, all particles were sieved with screens before being used as projectiles. The average diameter of the sand particles was 0.5 mm with a standard deviation of 0.02 mm. The quartz sand has a hardness of approximately 7 on the Mohs' scale whereas the hardness of LiF is 3.

A schematic drawing of the test equipment used is shown in figure 13. The setup was designed to feed sand particles into a stream of nitrogen gas. Compressed nitrogen gas was used as the carrier medium accelerating the projectiles to the desired velocity as they passed along a nozzle. The projectile velocity was controlled by the pressure of the nitrogen gas. The particle-nitrogen gas mixture was passed through a tube in order to obtain a relatively uniform beam of projectiles. The projectile velocities were measured by using double-flash exposure technique controlled by a time delay controller. The range of time gap between two flashes used in the present experiment was 0.1 - 10 m sec. Such a technique is considered to be more accurate than the rotating disc method developed by Ruff and Ives[72] for measuring projectile velocities. The specimens were held on an aluminum block at a distance of 2 cm below the exit end of the nozzle to allow clearance for the timing disc to pass between the nozzle and the specimen. The projectiles impacted at approximately normal incidence at a velocity in the range of 2.5 to 20 ms^{-1}

Figure 12. Standard Ottawa quartz sand grains used as projectiles for impact erosion.
(Average diameter: 0.5 mm)

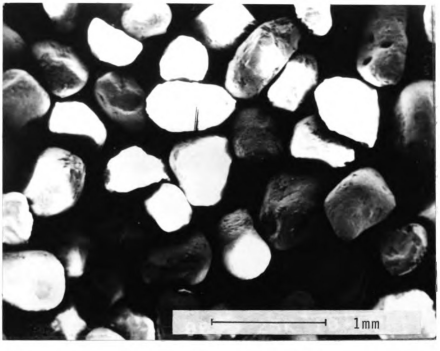
1mm

Figure 13. Schematic drawing of the erosion test setup.

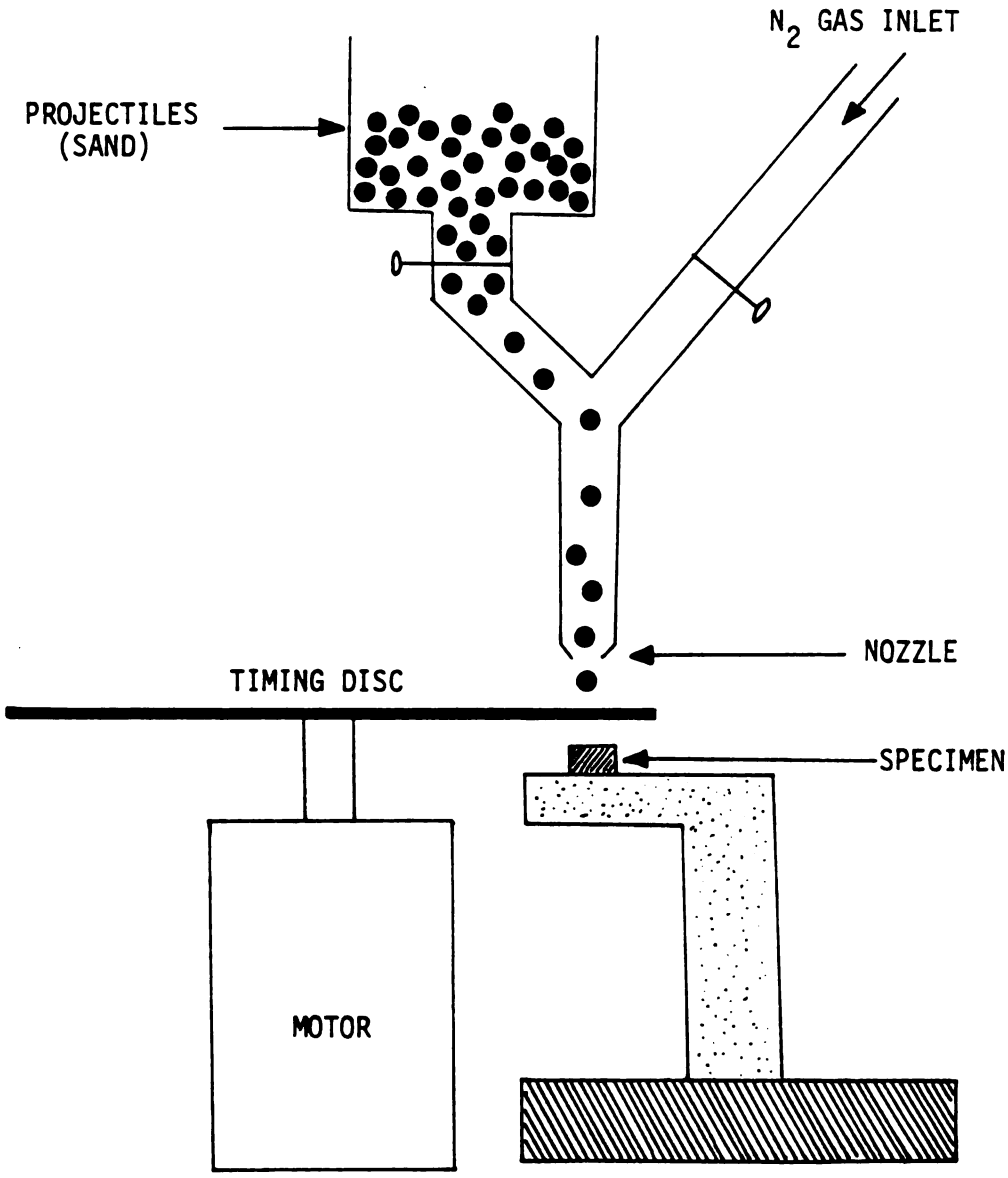
N_2 GAS INLET
PROJECTILES
(SAND)
NOZZLE
TIMING DISC
SPECIMEN
MOTOR

onto the cleaved (001) surfaces of the specimens. Exposure time for eroding was controlled by a timing disc with a 20^{o} wedge. It was rotated at a constant angular velocity of 11 RPM by using a motor. The range of the total exposure time was from 1 to 3 seconds. After eroding, the specimens were etched with a very dilute solution of ferric chloride in distilled water (10^{-4} molal solution) in order to reveal the dislocation etch pit patterns. These specimens were gold coated (about 100 Å) in a sputtering unit to make LiF specimens electrically conductive for SEM study. A slight pressure of argon gas was maintained in the chamber in order to improve the quality of gold coating.

3.3 Indentation Test

In order to compare the damage patterns due to particle impact with those produced by quasi-static indentation, indentation tests were also carried out. The impact damage observed by Evans and Wilshaw[18] in ZnS has been shown to be identical in form to that produced by quasi-static indentation, consisting of radial, lateral, and median cracks outside a plastic contact zone. A series of indentations, spaced 25 μm apart, were formed on (001) planes in the grain boundary region by means of 136^{o} Vickers diamond indenter using a micro-hardness tester. In one series, the indentations were made with one of the diagonals of the indenter parallel to the primary cleavage direction of the grain being indented. Three different loads (0.245, 0.735, 1.225 N) were used for the indentation. In another series, the diagonals of the indenter and primary cleavage directions made 45^{o} each other. After the size of the indentations had been measured, the specimens were etched and gold coated for SEM studies. The loading time used was about 10 seconds.

3.4 Microscopic Studies

By the etching procedure (15 to 20 seconds), grain boundaries and slip lines were revealed clear enough to be observed by optical and scanning electron microscopes. In addition to being a dislocation etchant, the etchant used preferentially dissolved material at fracture surfaces. This was helpful in revealing cracks that may be tightly sealed and be invisible during optical microscopy prior to etching. This characteristic of the etchant was helpful to reveal the very fine fracture patterns around the impact site.

Optical and scanning electron microscopic studies were helpful in determining fracture origins, estimation of the size and shape of the damages, and in observation of fracture paths. Enhanced depth of focus of SEM was helpful in studying the details of the damage in the impacted region. These details could not be resolved by optical microscopy.

In the following chapters, grain I refers to the grain in which impact or indentation occurred. Grain II refers to the grain adjacent to the grain I.

IV. RESULTS AND DISCUSSION

4.1 Damage Produced By Normal Impact Of Blunt Projectiles

Several interesting aspects of the deformation and fracture behavior of LiF bicrystals at high strain rates produced by blunt particle impact have emerged from the present investigations. A blunt projectile would be expected to produce a Hertzian stress field which has been proposed as a starting point for the analysis of impact erosion damage.[2] Such an analysis is related to the classical Griffith theory of fracture for elastic-brittle solids. Only normal impact method was used during this research since normal impact causes maximum erosion in a semi-brittle material as observed by Sheldon[25].

During the initial stages of the impact the target deforms elastically, and as the impact pressure continues to increase beyond the flow pressure of the target, the material deforms plastically.[27] When the impact occurs on the (001) surface, slip takes place on $\{110\}_{45}$o and $\{110\}_{90}$o planes which are inclined to the impacted surface at 45^{o} and 90^{o} respectively. According to Keh's model, {110} cracks are produced by the interactions of dislocations gliding on {110} planes. Such a fracture has been observed by Chaudhri et al[27] also. Low-velocity impacts on (001) surface of LiF produces only {110} cracks and (001) subsurface cleavage cracks.[27] As the impact velocity increases, (100) and (010) cleavage cracks are also initiated and the initiation point of these cracks is about 50-100 μm below the surface of the impact crater.[27]

Under the impact of a blunt projectile, very localized radial tensile stresses are generate in the contact zone, and these tensile stresses generate Hertzian cone cracks and give rise to the formation of (001)

cleavage cracks. By these stresses, some material is thrown upwards, normal to the specimen surface, at the same velocity as that of the rebounding projectiles.[27] So, very high projectile impact velocities cause material around the impact site to be detached from the crystal surface in the form of small fragments.

Diagrammatic representations of the top and sectional views of the major features of impact damage are shown in figure 14.

4.1.1 Damage produced by Normal Particle Impact on the Cleavage Planes in the Region away from the Grain Boundary

4.1.1.1 Crack Initiation and Propagation

The micrographs taken in a region away from the grain boundary represent the behavior of LiF single crystals under particle impact. The contact zone for a blunt projectile is characterized by massive plastic flow. Above the critical impact velocity, the damage is characterized by a contact zone from which a set of lateral fractures spread out. A typical crater and lateral fractures formed on (001) surface at impact velocities above 2.5 m/sec is shown in figure 15. Four main lateral fractures propagated along the crystallographic cleavage planes from the contact zone as evidenced by the linear shape and perpendicular angular relation between them. Although severe plastic flow and numerous microfractures occur inside the contact zone, usually four major lateral fractures along the {110} cleavage planes are developed outside the contact zone at low impact velocities. At normal impact in the region away from the grain boundary, the diameter of the contact zone increases linearly with increasing impact velocity as shown in figure 16. These results are very similar to those obtained by Schuon and Subramanian.[57] They found that the experimentally measured values of

Figure 14. Schematic drawings of the impacted damage on the (001) surface of LiF crystal (Ref. 27).

(A). Top view.

(B). Sectioned view.

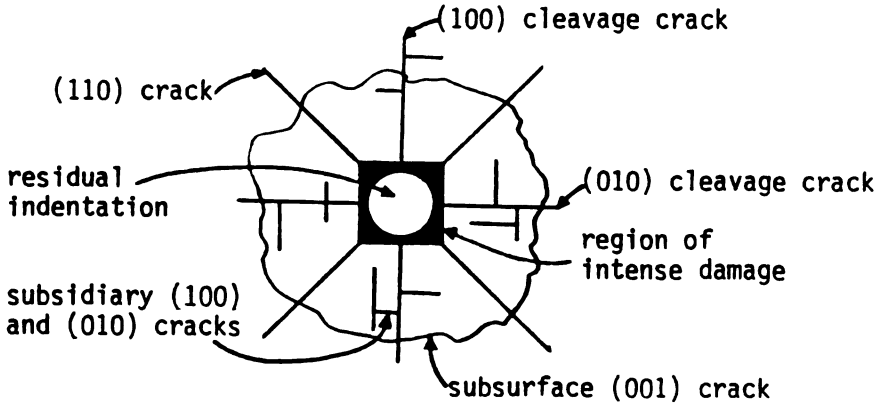
(100) cleavage crack
(110) crack
residual indentation
(010) cleavage crack
region of intense damage
subsidiary (100) and (010) cracks
subsurface (001) crack

(A)

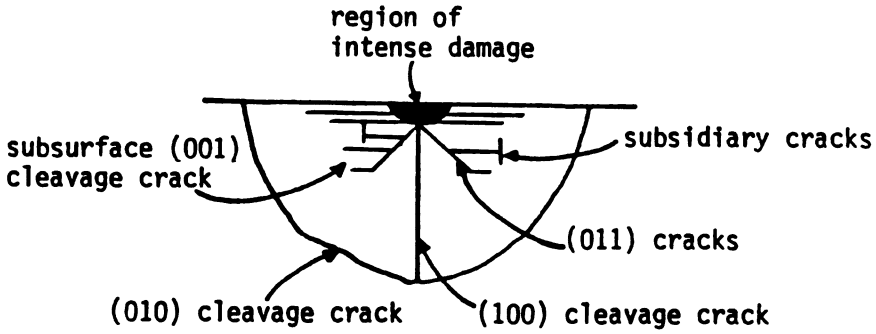
region of intense damage
subsurface (001) cleavage crack
subsidiary cracks
(011) cracks
(010) cleavage crack
(100) cleavage crack

(B)

Figure 15. A typical crater and lateral fractures formed on the (001) surface of LiF crystal by particle impact.

$\phi = 20^{o}$ $V = 11\ ms^{-1}$

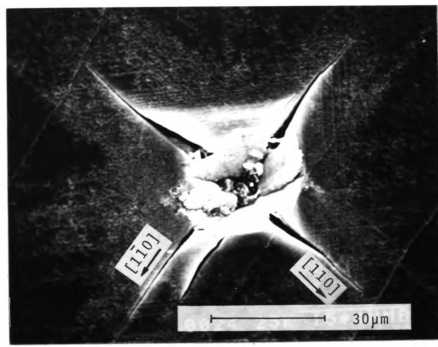
[1$\bar{1}$0]
[110]
30μm

Figure 16. Plot of the diameter of circle of contact as a function of the velocity of projectile.

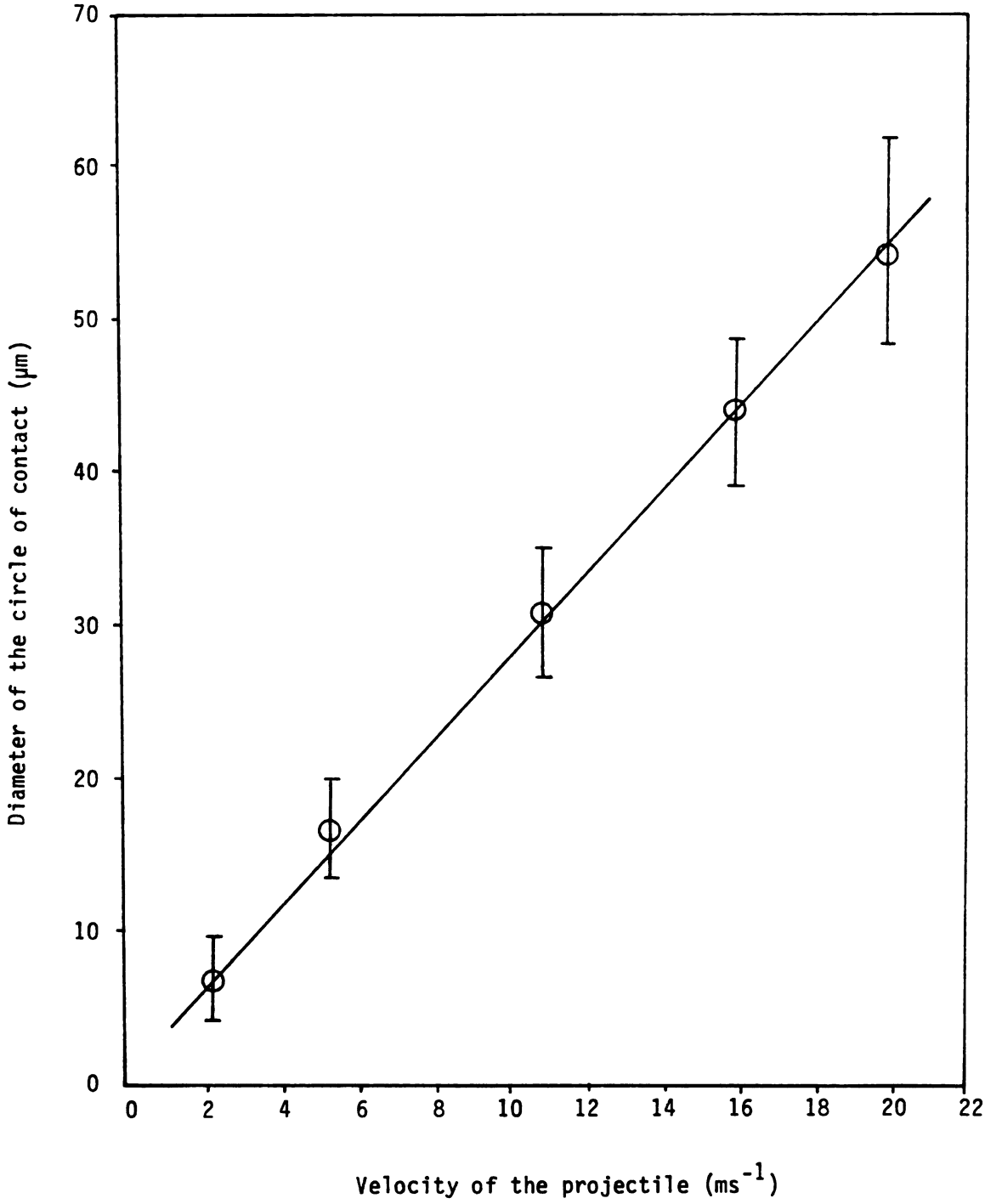
70
60
50
40
30
20
10
0
0
2
4
6
8
10
12
14
16
18
20
22
Diameter of the circle of contact (μm)
Velocity of the projectile (ms^{-1})

contact zone diameter are larger than the calculated values by a factor of about 10. These calculations were carried out by using Hertz's analysis. This discrepancy between theoretical and experimental values has been suggested by them to stem from the neglect of plastic deformation in the Hertz's analysis.

The length of lateral fractures also increases with increasing impact velocity as shown in figure 17 at velocities below 20 ms^{-1}. Schuon and Subramanian [55, 57] also found same tendency in single crystals of NaCl, KCl, and CaF_2 under particle impact. At higher velocities ranging from 50 to 200 ms^{-1}, Chaudhri et al found a tendency for the length of (110) lateral cracks to approach limiting value in LiF single crystals.[27]

In LiF crystals, three types of cleavage cracks could be nucleated by the interaction of slip dislocations. Stroh's model[73] is based on the coalescence of piled-up dislocation. In this model, a crack forms when the leading dislocations in a pile-up are forced to within a distance 'b' (magnitude of Burgers vector) of one another. Washburn's model[74], which is a modification of Cottrell's model[44], is associated with the interaction of dislocations contained in the slip planes intersecting perpendicularly each other. Keh's model[45] is associated with the interaction of dislocations contained in the slip planes intersecting each other with an angle of 120^{o}. The schematic illustrations of these three models are drawn in figure 18.

The Washburn's model can be represented by the following equation:

$$\frac{a}{2}[0\bar{1}1] + \frac{a}{2}[0\bar{1}\bar{1}] = a[0\bar{1}0] \quad . \tag{26}$$

This reaction does not result in a change of elastic energy;

$$\text{i.e.,} \quad b_1^2 + b_2^2 = b_3^2 \quad , \tag{27}$$

Figure 17. Plot of the length of lateral fracture as a function of the velocity of projectiles.

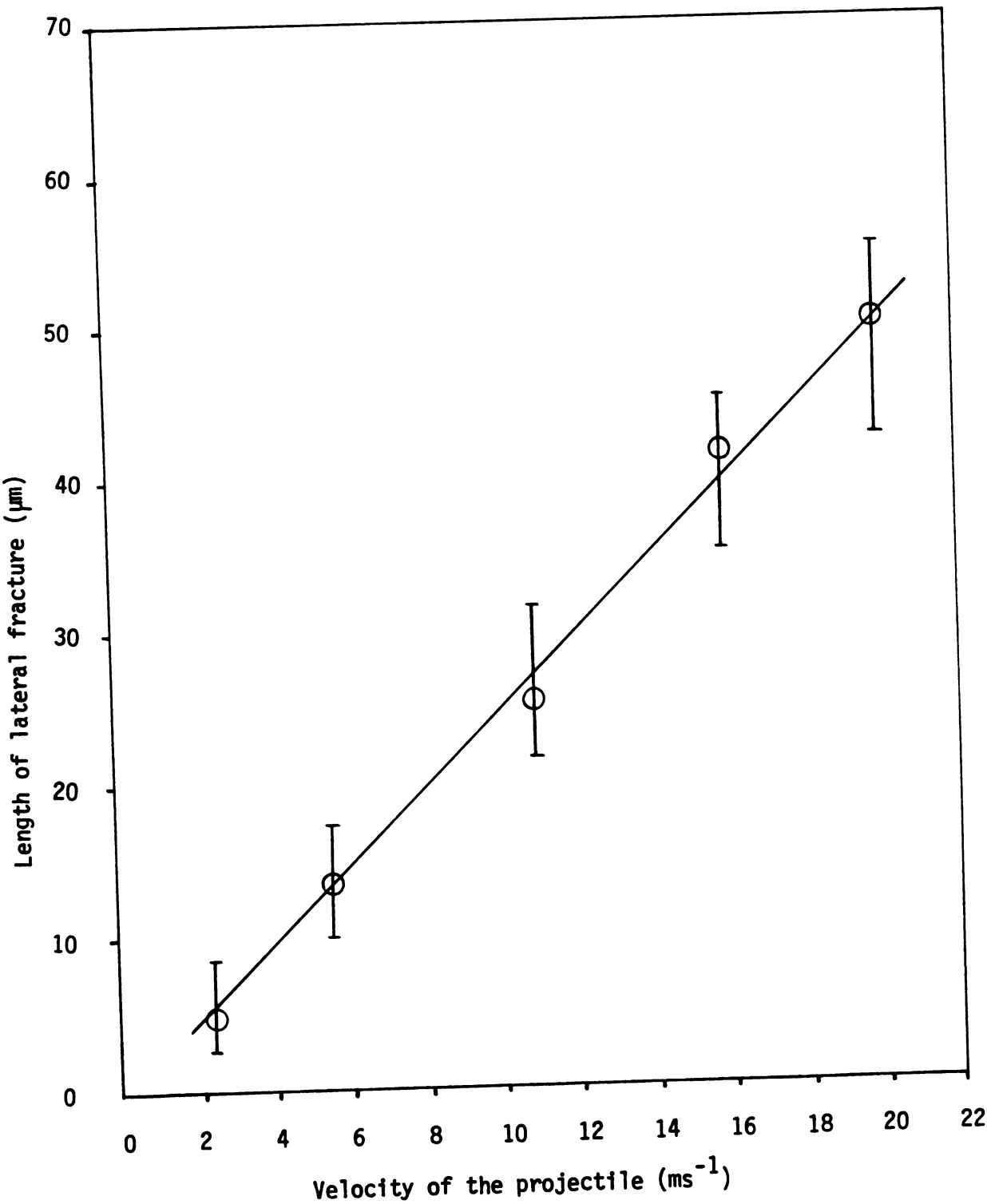
70
60
50
40
30
20
10
0
Length of lateral fracture (μm)
0
2
4
6
8
10
12
14
16
18
20
22
Velocity of the projectile (ms-1)

Figure 18. Schematic drawing of crack initiation mechanism by the interaction of dislocations.

(A). Stroh's model (Ref. 73)

(B). Washburn's model (Ref. 74)

(C). Keh's model (Ref. 45)

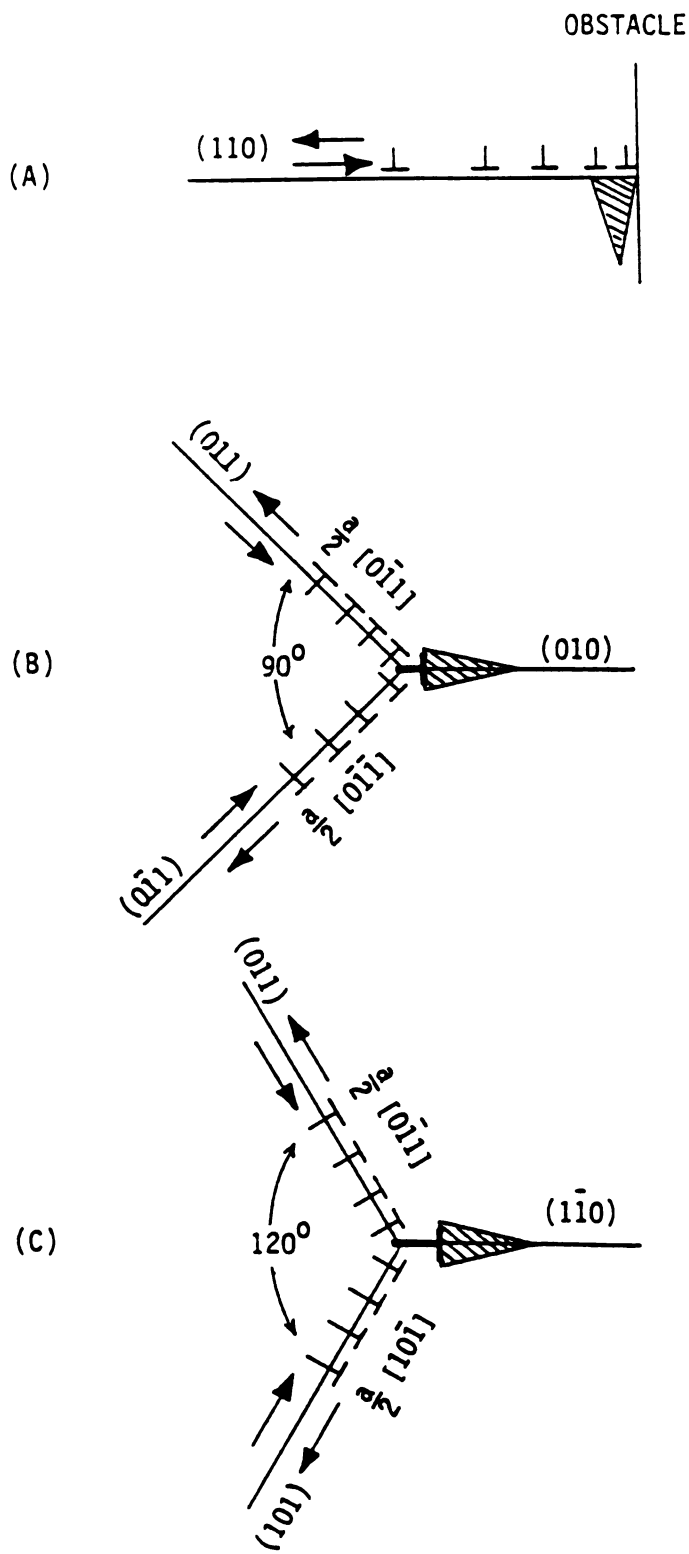
OBSTACLE
(A)
(110)
(B)
(011)
$\frac{a}{2}$ [0$\bar{1}$1]
90°
(010)
$\frac{a}{2}$ [0$\bar{1}$1]
(a$\bar{1}$1)
(C)
(011)
$\frac{a}{2}$ [0$\bar{1}$1]
120°
(1$\bar{1}$0)
$\frac{a}{2}$ [10$\bar{1}$]
(101)

where, $\underline{b}_1 = \frac{a}{2}[0\bar{1}1]$,

$\underline{b}_2 = \frac{a}{2}[0\bar{1}\bar{1}]$,

and $\underline{b}_3 = a[0\bar{1}0]$.

Washburn's model can be applied for the interaction of dislocations contained in the {110} slip planes intersecting perpendicularly each other, such as (001) plane with $(0\bar{1}1)$ plane,and (101) plane with $(10\bar{1})$ plane. As can be seen in figure 18(B), cracks are initiated on {100} type primary cleavage planes in Washburn's model.

Similarly, Keh's model can be represented by the following equation.

$$\frac{a}{2}[0\bar{1}1] + \frac{a}{2}[10\bar{1}] = \frac{a}{2}[1\bar{1}0] \quad . \tag{28}$$

In this reaction, half of the elastic energy is released by the dislocation interaction, i.e., $b_1^2 + b_2^2 = 2b_3^2$, (29)

where $\underline{b}_1 = \frac{a}{2}[0\bar{1}1]$,

$\underline{b}_2 = \frac{a}{2}[10\bar{1}]$,

and $\underline{b}_3 = \frac{a}{2}[1\bar{1}0]$.

Therefore, reaction (28) is more favorable than reaction (26). Keh's model can be applied in the interaction of dislocations contained in the {110} slip planes intersecting each other with an angle of 120^o such as (011) plane with $(10\bar{1})$ plane, (011) plane with (101) plane, $(0\bar{1}1)$

plane with $(10\bar{1})$ plane, and $(0\bar{1}1)$ plane with (101) plane. By considering the edge and screw components of the individual dislocations, reaction (28) can be rewritten as following:[74]

$$\frac{a}{2}[0\bar{1}1] + \frac{a}{2}[10\bar{1}] = (\frac{a}{6}[2\bar{1}1]_{edge} + \frac{a}{3}[\bar{1}\bar{1}1]_{screw})$$

$$+ (\frac{a}{6}[1\bar{2}\bar{1}]_{edge} + \frac{a}{3}[11\bar{1}]_{screw})$$

$$= (\frac{a}{6}[2\bar{1}1]_{edge} + \frac{a}{6}[1\bar{2}\bar{1}]_{edge})$$

$$+ (\frac{a}{3}[\bar{1}\bar{1}1]_{screw} + \frac{a}{3}[11\bar{1}]_{screw})$$

$$= \frac{a}{2}[1\bar{1}0] + 0 \quad . \qquad (30)$$

Thus, the two screw components cancel each other and the two edge components combine together. Therefore the elastic energy due to the coalescence of the screw components is released. The resultant dislocation line vector $\frac{1}{2}a[1\bar{1}0]$ lies on the (112) plane.[74] This dislocation is immobile since (112) plane is not a slip plane in LiF crystal due to its higher Peierls-Nabarro force than that of {110} planes. Therefore, the dislocations generated on the two intersecting slip planes (011) and (101) pile up against this immobile dislocation and initiate a crack in the $(1\bar{1}0)$ plane as shown in figure 18(C). The intersections of these cracks with the (001) surface are along <110> directions, as

evidenced by the four lateral fractures propagated along <110> directions as indicated in figure 19. These four lateral fractures which are formed along the <110> directions are associated with Keh's model. Since LiF has cubic symmetry, there are four {110} planes of symmetry for blunt projectiles impacting in the [001] direction onto the (001) surface. As can be observed in the micrographs presented in figure 19, this type of lateral fractures along the <110> directions are the dominant feature of crack propagation caused by the particle impact on (001) surfaces. Moreover, the directions of these dominant lateral fractures coincide with those of the leading edge dislocation etch pits which are formed along <110> directions on the $\{110\}_{90}$o slip planes. The fact that these lateral fractures lie in the $\{110\}_{90}$o planes can be also confirmed easily by chemically polishing down the specimen surface and examining the cracks underneath.

Occasionally, lateral fractures along the <100> directions were also observed, indicating that crack nucleation according to Washburn's model, along {100} primary cleavage planes was also operative.[74] This feature can be observed in figure 20. Primary {100} cleavage planes made 45^{o} with secondary {110} cleavage planes. Such a lateral fracture along {100} can be also formed by the mode I crack mechanism due to the crack opening tensile stress caused by the particle impact and crater formation process.

In crystals with strong cleavage tendencies, there is some compromise between the tendencies for cracks to follow stress trajectories and to follow cleavage planes. Crystallographic nature of cleavage and the presence of Hertzian stress field results in a compromise in crack propagation; fracture occurs along the non-cleavage surfaces as well as along the cleavage planes due to this compromise, as can be observed in figure 21. Such non-cleavage cracks were never observed in LiF bicrystals

Figure 19. Craters and lateral fractures formed due to the particle impact on the (001) surface of LiF crystal.

(A). $\phi = 20^{o}$ $V = 20\ ms^{-1}$

(B). $\phi = 30^{o}$ $V = 16\ ms^{-1}$

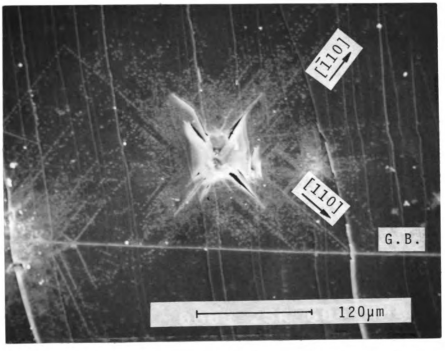

(A)

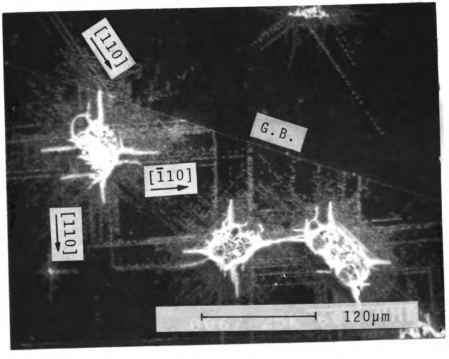

(B)

Figure 20. Lateral fractures propagating along {100} planes as well as along {110} planes due to particle impact on the (001) surface of LiF crystal.

$\phi = 20^{o}$ $V = 5.5\ ms^{-1}$

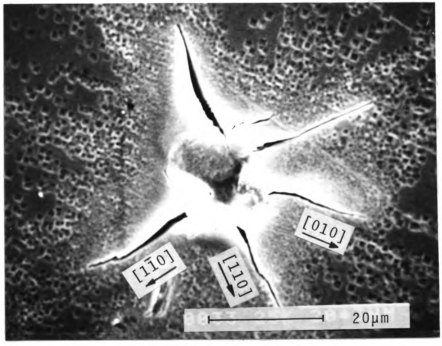
[010]
[1$\bar{1}$0]
[$\bar{1}$10]
20μm

Figure 21. Crater and lateral fractures in LiF single crystals due to particle impact on the (001) surface. Continuation of lateral fractures along non-cleavage surfaces as well as along the cleavage planes, due to the compromise between the Hertzian stress field and crystallographic nature of the specimen can be observed in this figure.

$\phi = 20^{o}$ $V = 20\ ms^{-1}$

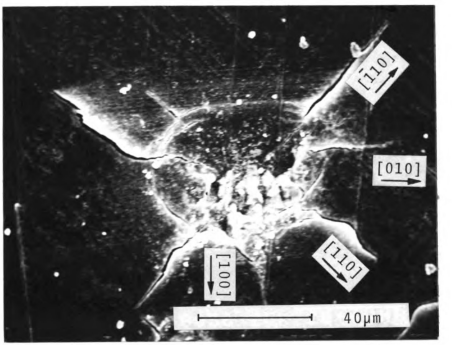
[110]
[010]
[110]
[100]
40μm

under mode I crack propagation due to its strong anisotropic character as analyzed by Lee and Subramanian.[71]

4.1.1.2 Slip Propagation

According to Keh[60], all dislocation lines formed by indentation on (001) surface of MgO single crystal lie in the {110} primary slip planes, and the leading edge dislocations propagate along <110> directions on the $\{110\}_{90}$o slip planes under such conditions.

In case of particle impact on (001) surface of LiF bicrystal, etch pit patterns similar to those obtained by Keh were observed as shown in figure 22, since LiF and MgO have the same crystal structure. Specifically, these two planes are (110) and $(1\bar{1}0)$ planes. The fact that the leading edge dislocations propagate along <110> directions can be easily confirmed by measuring the angles between slip lines and the {100} primary cleavage planes formed by cleaving with chisel and hammer.

In addition to the two $\{110\}_{90}$o slip planes, four $\{110\}_{45}$o slip planes are also activated due to the shear stress caused by particle impact as can be observed in figure 23. The presence of all these slip systems produces a characteristic "rosette" pattern as presented in figure 23. In this micrograph, the rosette pattern is symmetric since the direction of impact site is normal to the surface and the grain boundary is far from the impact site.

4.1.2 Damage produced by normal particle impact on the cleavage planes near the grain boundary

4.1.2.1 Crack Initiation and Propagation

When the plastic deformation is confined essentially to planar slip, grain boundaries exert a strong influence on the flow stress and the

Figure 22. Slip on {110} planes due to the particle impact on the (001) surface of LiF bicrystal.

$\phi = 20^{o}$ $V = 20\ ms^{-1}$

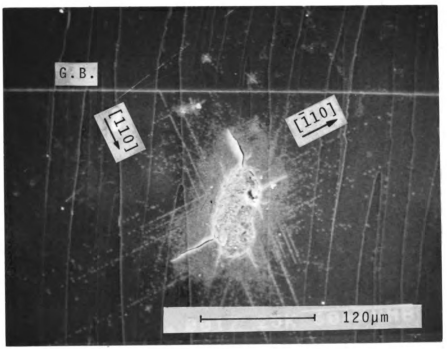
G.B.
[110]
[110]
120μm

Figure 23. Slip lines formed along $\{110\}_{45}$o slip planes as well as along $\{110\}_{90}$o planes by particle impact on the (001) surface of LiF bicrystal.

$\phi = 6^{o}$ $V = 2.5\ ms^{-1}$

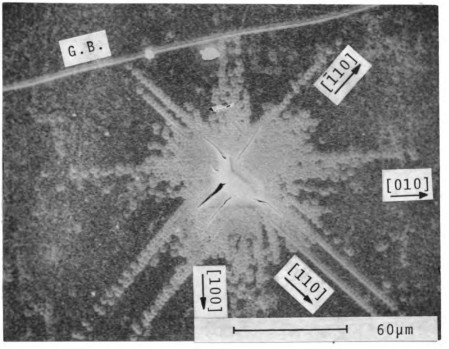
G.B.
[110]
[010]
[001]
[110]
60μm

fracture behavior.[65] Westwood[68] concluded from the observations on MgO bicrystals that cracks may be nucleated at a low angle grain boundary through the superposition of the tensile stress field of two dislocation pile-ups generated on both sides of the boundary.

In this present study, impact load is applied only on one grain since the particle size is much smaller than the size of each grain. Due to the existence of grain boundary near the impact site and the Hertzian stress field introduced by the particle impact near the grain boundary, the shapes of craters and lateral fractures are more complicated as compared to those formed by particle impact in a region away from the grain boundary.

As can be seen in figure 24, some lateral fractures are blocked by the grain boundary indicating the strong influence of the crystallographic misorientation on crack propagation. In bicrystal specimens having small tilt angle, such blockage was observed less frequently than in the case of the specimens having large tilt angle, implying that the resistance of grain boundary against the crack propagation increases as the magnitude of tilt angle increases.

When the impact occurred in a region close enough to the grain boundary, transcrystalline crack propagation was also observed in addition to the blockage of lateral fractures as can be observed in figure 25. In figure 25, one crack which was initiated along the (110) cleavage plane in grain I propagated across the grain boundary into the grain II along the (100) primary cleavage plane. As can be seen in figure 26, most of the lateral fractures propagated across the grain boundary when the particle impact occurred in a region very close to the grain boundary.

Figure 24. Lateral fractures due to the particle impact blocked by the grain boundary.

$\phi = 30^{o}$ $V = 11\ ms^{-1}$

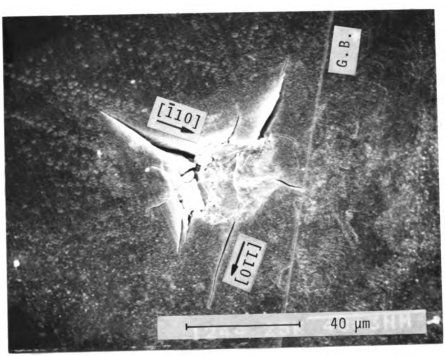
G.B.
[1$\bar{1}$0]
[01$\bar{1}$]
40 μm

Figure 25. Interaction of lateral fractures caused by particle impact with grain boundary. Lateral fractures that are blocked by the grain boundary as well as those that propagate through the grain boundary can be seen in these micrographs.

(A). $\phi = 15^{o}$ $V = 5.5\ ms^{-1}$

(B). $\phi = 30^{o}$ $V = 20\ ms^{-1}$

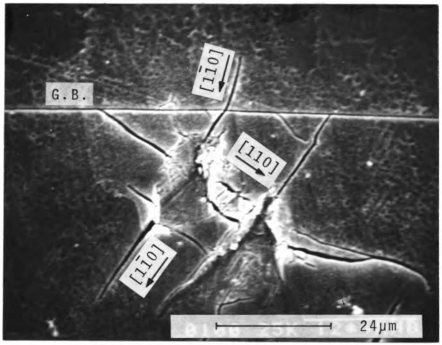

(A)

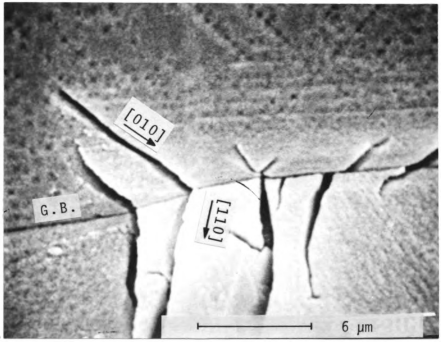

(B)

Figure 26. Lateral fractures due to the particle impact in a region very close to grain boundary. In this case, the lateral fractures propagated across the grain boundary.

$\phi = 45^{o}$ $V = 11\ ms^{-1}$

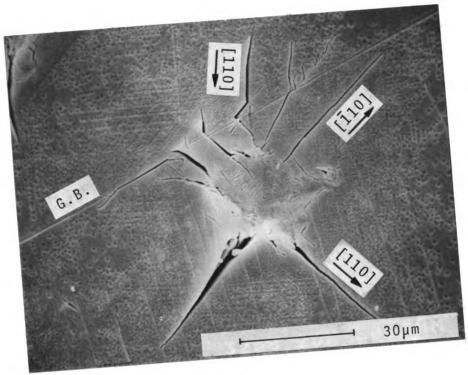
[110]
[1$\bar{1}$0]
G.B.
[11$\bar{1}$]
30μm

In some cases, as shown in figure 27, cracks also initiated along the (100) primary cleavage plane in addition to the (110) cleavage in grain I and propagated along the (100) plane in grain II implying that direction of crack propagation is based on which cleavage plane the resolved normal stress first reaches the fracture stress of that plane.

Under particle impact, intercrystalline crack propagation was also observed in addition to the transcrystalline crack propagation, as can be observed in figure 28. In this case, the resolved normal stress on grain boundary should have first reached the fracture stress of grain boundary surface. Although LiF shows very strong cleavage tendencies at room temperature, intercrystalline crack propagation is also possible due to the dynamic loading conditions and stress concentration at the grain boundary.

In some cases, crack branching was also observed as can be seen in figure 29. Due to the existence of grain boundary near the impact site, one non-cleavage crack (marked '*') was initiated in grain I and propagated toward the grain boundary. This non-cleavage crack made two branches along the (110) and (100) cleavage planes. The direction of (110) cleavage crack coincides with the $[1\bar{1}0]$ primary slip direction, and the two branched lateral fractures make 45^{o}.

Multiple cracks were also initiated in the adjacent grain from the grain boundary under the particle impact as can be observed in figure 30. By recognizing that these multiple cracks are not in contact with cracks formed by particle impact, one can conclude that these multiple cracks are formed by the tensile stress components in the Hertzian stress field introduced by particle impact.

Occasionally, when particle impact occurred exactly on the grain

Figure 27. Cracks initiated along the {100} primary cleavage planes in addition to the {110} cleavage cracks.

$\phi = 30^{o}$ $V = 20\ ms^{-1}$

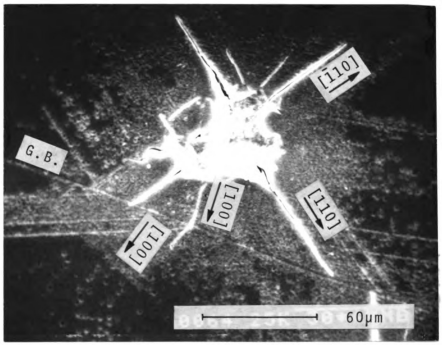
G.B.
[100]
[100]
[011]
[011]
60μm

Figure 28. Intercrystalline and transcrystalline crack propagation under particle impact.
(A). $\phi = 20^{o}$ $V = 20\ ms^{-1}$
(B). Magnified view of (A).

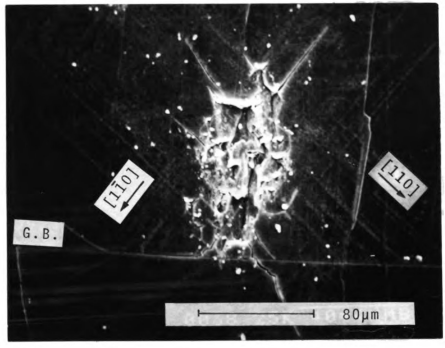

(A)

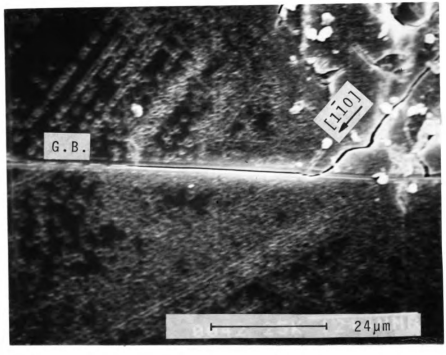

(B)

Figure 29. Crack branching in a specimen eroded by particle impact on (001) plane.

(A). $\phi = 30^{o}$ $V = 11\ ms^{-1}$

(B). Magnified view of (A).

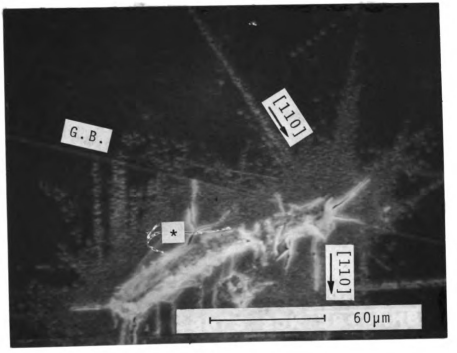

(A)

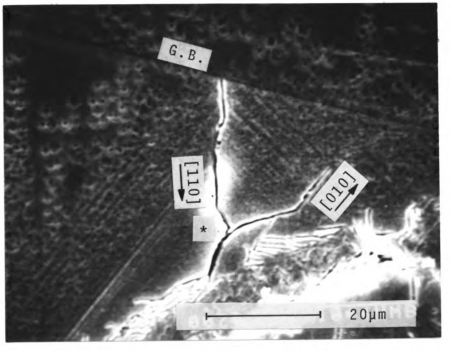

(B)

Figure 30. Discontinuous multiple cracks initiated in adjacent grain from the grain boundary under the particle impact.

$\phi = 20^{o}$ $V = 20\ ms^{-1}$

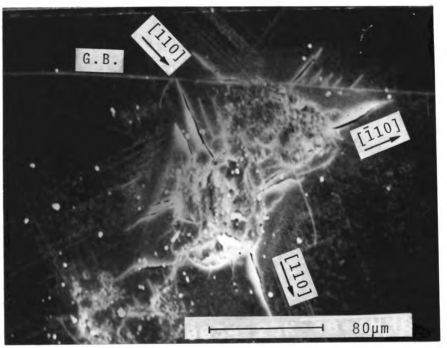
G.B.
[110]
[$\bar{1}$10]
[1$\bar{1}$1]
80μm

boundary as can be observed in figure 31, two sets of lateral fractures along the {110} planes were observed in each grain. Microfracture within the region of contact is extensive as can be observed in figure 31(B). These microfractures departed from cleavage planes and produced numerous microcrystals. During plastic flow, these microcrystals may become reoriented and possibly form curved boundaries.

4.1.2.2 Mechanism of Material Removal under Particle Impact

The main mechanism of material removal under impact erosion is the intersection of lateral fracture with another lateral fracture or grain boundary.

Lateral fractures propagate radially outward from the impact site without any intersections between them. Therefore, material loss was seldom observed during single impact by blunt projectiles on LiF single crystals. Material removal under such cases usually occurs by multiple impact.[57] On the other hand, even one single impact on LiF bicrystals can produce material loss as can be observed in figures 32-34. In the case of the impact damage shown in figure 32, severely curved lateral fractures aid material removal process. Such lateral fractures form due to the presence of grain boundary near the impact site and stress distribution caused by dynamic loading near the grain boundary. Such a feature has never been observed in a region away from the grain boundary during the course of this investigation.

In the case of the impact damage shown in figure 33, lateral fractures intersected with grain boundary resulting in material removal. Such a feature emphasizes the important role of grain boundaries on material removal during particle impact. The segment in figure 33(B) (marked '*') is an example for such a mechanism of material loss.

Figure 31. Lateral fractures and microfractures formed by particle impact on the grain boundary.

(A). $\phi = 30^{o}$ $V = 11\ ms^{-1}$

(B). $\phi = 15^{o}$ $V = 11\ ms^{-1}$

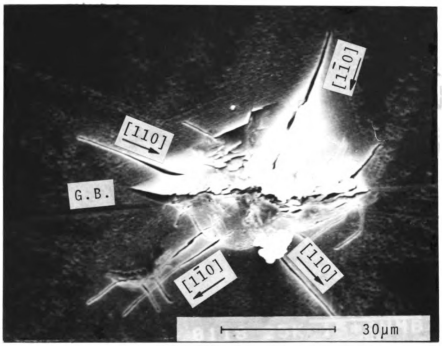

(A)

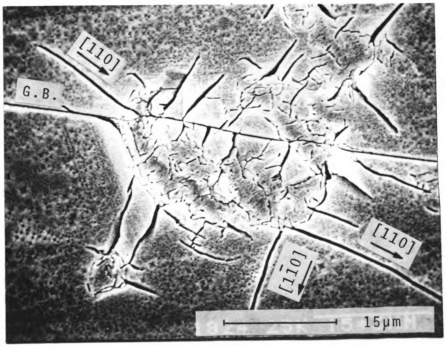

(B)

Figure 32. Severely curved lateral fractures formed by particle impact near the grain boundary.
(A). $\phi = 30^{o}$ $V = 16\ ms^{-1}$
(B). $\phi = 30^{o}$ $V = 11\ ms^{-1}$

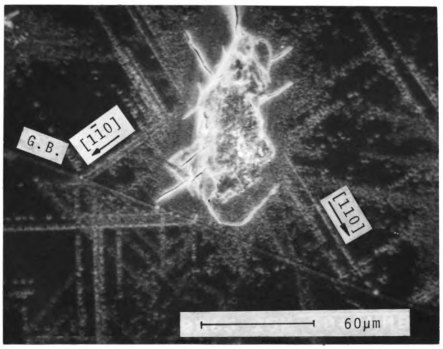

(A)

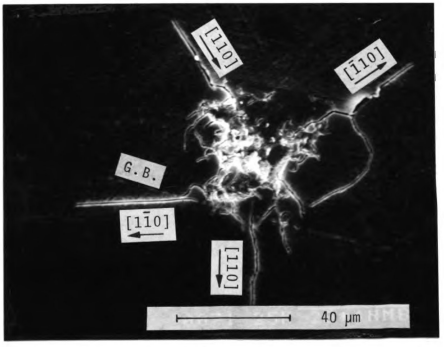

(B)

Figure 33. Lateral fractures intersecting with grain boundary causing material removal. The segment (marked '*') in these figures are the examples for such a mechanism of material loss.

(A). $\phi = 1^{o}$ $V = 11\ ms^{-1}$

(B). $\phi = 15^{o}$ $V = 16\ ms^{-1}$

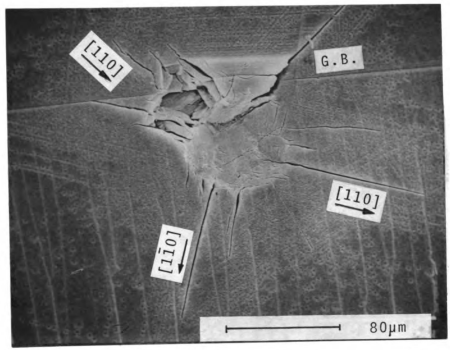

(A)

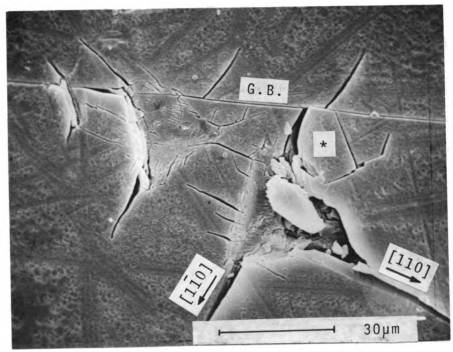

(B)

Intersection of lateral fractures with cleavage cracks along the $\{110\}_{45}$o plane is also another possible mechanism for the material removal as can be identified in figure 34. Such a mechanism can also occur in a region away from the grain boundary.

Material loss occurs both during the loading and unloading parts of the impact.[27] During loading, material flows plastically along $\{110\}_{45}$o slip planes. At high velocities the inertia of this deformed material causes material removal during the rebound of projectiles.

4.1.2.3 Direction of Crack Propagation

The condition which determines the extension of a crack can be expressed in terms of the total energy for a quasi-static system.[41]

$$U = (-W_L + U_E) + U_S \quad , \tag{31}$$

where W_L is the work of the applied forces,

U_E is the elastic strain energy in the cracked body, and

U_S is the total surface energy.

Since $(-W_L + U_E)$ decreases while U_S increases with crack extension, an energy interchange occurs between them. The variation of the energy terms becomes as following with respect to crack area (C).

$$\frac{du}{dc} = \frac{d\,(-W_L + U_E)}{dc} + \frac{dU_S}{dc} \quad ,$$

$$= -G + 2\gamma \quad , \tag{32}$$

where G is the mechanical energy release-rate and γ is the fracture

Figure 34. Intersection of lateral fractures with cleavage cracks along the $\{110\}_{45^o}$ cleavage plane resulting in material removal (indicated by '*').

$\phi = 1^o$ $V = 11\ ms^{-1}$

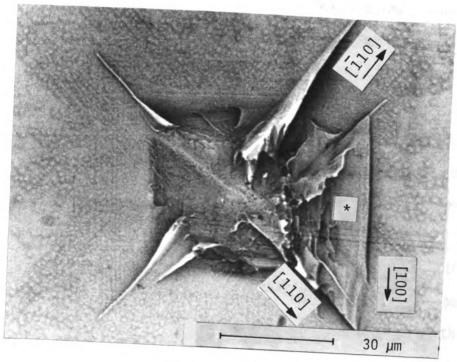
[1̄10]
[110]
[100]
30 µm

surface energy.

Cracks tend to propagate along trajectories of lesser principal stresses, thereby maintaining near-orthogonality to a major component of tension.[75] For an ideally brittle solid, the relative orientation of an incremental extension dc is that which maximizes the quantity $(G-2\gamma)$. For anisotropic solids, it is necessary to take into account the orientation dependence of both elastic constants and surface energy in determining maxima in $(G-2\gamma)$. Clearly, in crystals with strong cleavage tendencies the anisotropy in γ will govern the direction of crack propagation.[41] However, some compromise occurs between the tendencies for cracks to follow stress trajectories and cleavage planes.

According to the Sohncke's[76] normal stress law for the brittle fracture, the cleavage of a single crystal occurs when the resolved normal stress on the cleavage plane reaches a critical value. Such feature of brittle fracture was fully identified in a model established experimentally by Lee and Subramanian[71] using LiF bicrystals. In that study, mode I loading method was used for the initiation of cleavage crack. This method is extended in this investigation in order to analyze the crack propagation mechanism under impact loading since the specimens are very similar although the damage patterns produced by particle impact are much more complicated than those obtained by mode I loading method.

By particle impact, let primary or secondary cleavage cracks be initiated and propagated in grain I. When these cracks reach the grain boundary, the mode of fracture in the adjacent grain, grain II, will depend on which plane the resolved normal stress for fracture is reached first.

Based on the crystal structure of LiF and seed setting, grain II

has two potential primary cleavage planes, (100) and (010), and two potential secondary cleavage planes, (110) and $(1\bar{1}0)$, along which the (100) cracks initiated in grain I could propagate as illustrated in figure 35. Cracks can also propagate along the grain boundary surface as well as cleavage planes depending upon the misorientation angles and the orientation of grain boundary with respect to the approaching crack path. Thus, crack propagation direction is decided depending on which fracture plane (or boundary) the resolved normal stress first reaches the fracture stress of the plane (or boundary).

By assuming that tensile stress σ_g is developed at grain boundary when the crack tip approaches the grain boundary along (100) plane in grain I in which impact occurred, the resolved normal stresses of σ_g on cleavage planes and grain boundary are obtained. When this resolved normal stress reaches the critical normal (fracture) stress of one of the above planes, crack will propagate along that plane.

Equations for the homogeneous continuum can be assumed to be applicable in this region because grain boundary has weak anisotropic character and its thickness is extremely small ($\lesssim$20 Å).

$$\sigma_{(100)} = \sigma_g \cos^2 \phi \quad , \tag{33}$$

$$\sigma_{(010)} = \sigma_g \cos^2 (90^\circ - \phi) \quad , \tag{34}$$

$$\sigma_{(110)} = \sigma_g \cos^2 (45^\circ - \phi) \quad , \tag{35}$$

Figure 35. Schematic drawing of specimen surface illustrating potential crack propagation directions for the case of {100} crack interaction with grain boundary. Specimen surface is (001) in both grains.

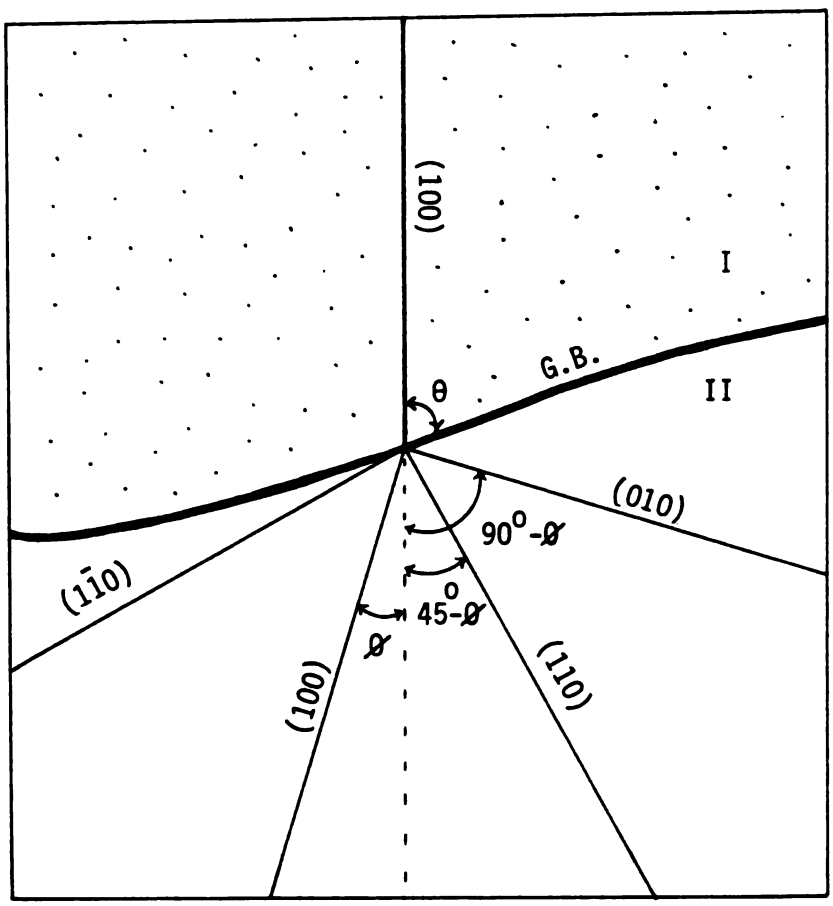
(100)
I
G.B.
θ
II
(010)
90°-ø
(1$\bar{1}$0)
45°-ø
ø
(100)
(110)

$$\sigma_{(1\bar{1}0)} = \sigma_g \cos^2 (45^o + \phi) \quad , \tag{36}$$

and $$\sigma_{gb} = \sigma_g \cos^2 \theta \quad , \tag{37}$$

where $\sigma_{(110)}$, $\sigma_{(010)}$, $\sigma_{(110)}$, and $\sigma_{(1\bar{1}0)}$ are the fracture stresses of the corresponding cleavage planes and σ_{gb} is the fracture stress of the grain boundary.

According to the crystal structure and seed setting, the range of misorientation angle is $0^o < \phi \leq 45^o$. Thus, as can be seen clearly in figure 35, in this range

$$\phi < 90^o - \phi \quad , \tag{38}$$

and

$$\cos^2 \phi > \cos^2 (90^o - \phi) \quad . \tag{39}$$

Therefore, the transcrystalline crack propagation along the primary cleavage plane occurs only along the (100) plane in grain II because the resolved normal stress on (100) plane is larger than that for (010) plane under such conditions.

Similarly, for the case of secondary cleavage,

$$45^o - \phi < 45^o + \phi \quad , \tag{40}$$

and

$$\cos^2 (45^o - \phi) > \cos^2 (45^o + \phi) \quad . \tag{41}$$

Therefore, the resolved normal stress on (110) plane is larger than that for $(1\bar{1}0)$ plane. Consequently, the transcrystalline crack propagation along the secondary cleavage plane occurs only along the (110) plane.

As a result, (100) cleavage crack initiated in grain I can propagate by one of the following three modes: transcrystalline fracture along the (100) primary cleavage plane in grain II, transcrystalline fracture along the (110) secondary cleavage plane in grain II, or intercrystalline fracture. When the critical normal stress exceeds the fracture stress of that plane, crack propagates along that plane. Fracture stress of each plane can be calculated by using surface energies of these planes or grain boundary energy.

From Hooke's law, the equation relating the fracture stress and surface energy can be written as following.

$$\sigma_f = \sqrt{\frac{E\gamma}{a_o}} \tag{42}$$

where, σ_f is fracture stress,

E is Young's modulus,

γ is surface energy, and

a_o is lattice constant.

By substituting the constants of LiF ($E = 10.2 \times 10^{11}$ dyne/cm^2, $a_o = 4.027 \times 10^{-8}$ cm) and the surface energy values[71] of LiF ($\gamma_{\{100\}}$ = 520 ergs/cm^2, $\gamma_{\{110\}}$ = 2,000 ergs/cm^2, γ_{gb} = 940 ergs/cm^2) into the equation (42), the fracture stress needed for separation is calculated and the values are listed in table 2.

From the values shown in table 2,

Table 2. Calculated values of fracture stress of LiF crystal (Ref. 71)

unit : N/m^2

Primary cleavage plane	1.15×10^{10}
Secondary cleavage plane	2.25×10^{10}
Grain boundary	1.54×10^{10}

$$\sigma_{(100)} = 0.746 \ \sigma_{gb} \quad , \tag{43}$$

$$\sigma_{(110)} = 1.461 \ \sigma_{gb} \quad , \text{ and} \tag{44}$$

$$\sigma_{(100)} = 0.511 \ \sigma_{(110)} \quad . \tag{45}$$

From the equations (33), (37), and (43) the condition for transcrystalline crack propagation along the primary cleavage plane (instead of intercrystalline fracture) is

$$\cos^2 \phi < 0.746 \cos^2 \theta \quad , \tag{46}$$

and the condition for intercrystalline fracture is

$$\cos^2 \phi > 0.746 \cos^2 \theta \quad . \tag{47}$$

Likewise, from the equations (35), (37), and (43) the condition for transcrystalline crack propagation along the secondary cleavage plane instead of intercrystalline fracture is

$$\cos^2 (45^0 - \phi) < 1.461 \cos^2 \theta \quad , \tag{48}$$

and the condition for intercrystalline fracture is

$$\cos^2 (45 - \phi) > 1.461 \cos^2 \theta \quad . \tag{49}$$

The orientation of grain boundary with respect to the approaching crack path does not have any effect on the determination of crack propagation

along the primary or secondary cleavage planes in grain II. Therefore, from the equations (33), (35), and (45), the condition for crack propagation along the (100) cleavage plane, instead of (110) cleavage, is

$$\cos^2 \phi < 0.511 \cos^2 (45^o - \phi) \quad . \tag{50}$$

Similarly for secondary cleavage, instead of primary (100) cleavage,

$$\cos^2 \phi > 0.511 \cos^2 (45^o - \phi) \quad . \tag{51}$$

These six conditions for the determination of crack path were drawn and superimposed in figure 36. In this figure, TR. I, TR. II, and INT. indicate the zones for the transcrystalline cleavage along the primary cleavage plane, transcrystalline cleavage along the secondary cleavage plane, and intercrystalline fracture, respectively.

The three curves of figure 36 represent the various combinations of critical angles (θ and ϕ) for which two different modes of crack propagation can occur simultaneously. The critical value of ϕ is 44.4^o at which transcrystalline cleavage could occur along the primary cleavage plane or secondary cleavage plane. When the tilt angle (ϕ) is smaller than 30.3^o, only primary cleavage fracture occurs regardless of the value of the angle of relative grain boundary orientation (θ). For the values of θ ranging from 34.2^o to 90^o. primary cleavage always occurs provided ϕ is smaller than 44.4^o. For the values of θ ranging 0^o to 34.2^o, primary cleavage occurs provided ϕ is smaller than the corresponding critical angles, ranging from 30.3^o to 44.4^o. As can be seen in figure 36, the dominant crack propagation mode, when (100) crack interacts with a grain boundary is transcrystalline crack propagation along the (100) cleavage

Figure 36. Crack propagation mode for various ϕ and θ when (100) crack in grain I interacts with a tilt boundary. (ϕ is tilt angle and θ is the angle between crack path in grain I and grain boundary)

● : Transcrystalline crack propagation along promary cleavage plane,

■ : Transcrystalline crack propagation along secondary cleavage plane,

▲ : Intercrystalline crack propagation,

IN. : Intercrystalline crack propagation zone,

TR.I.: Transcrystalline(primary) crack propagation zone, and

TR.II.: Transcrystalline(secondary) crack propagation zone.

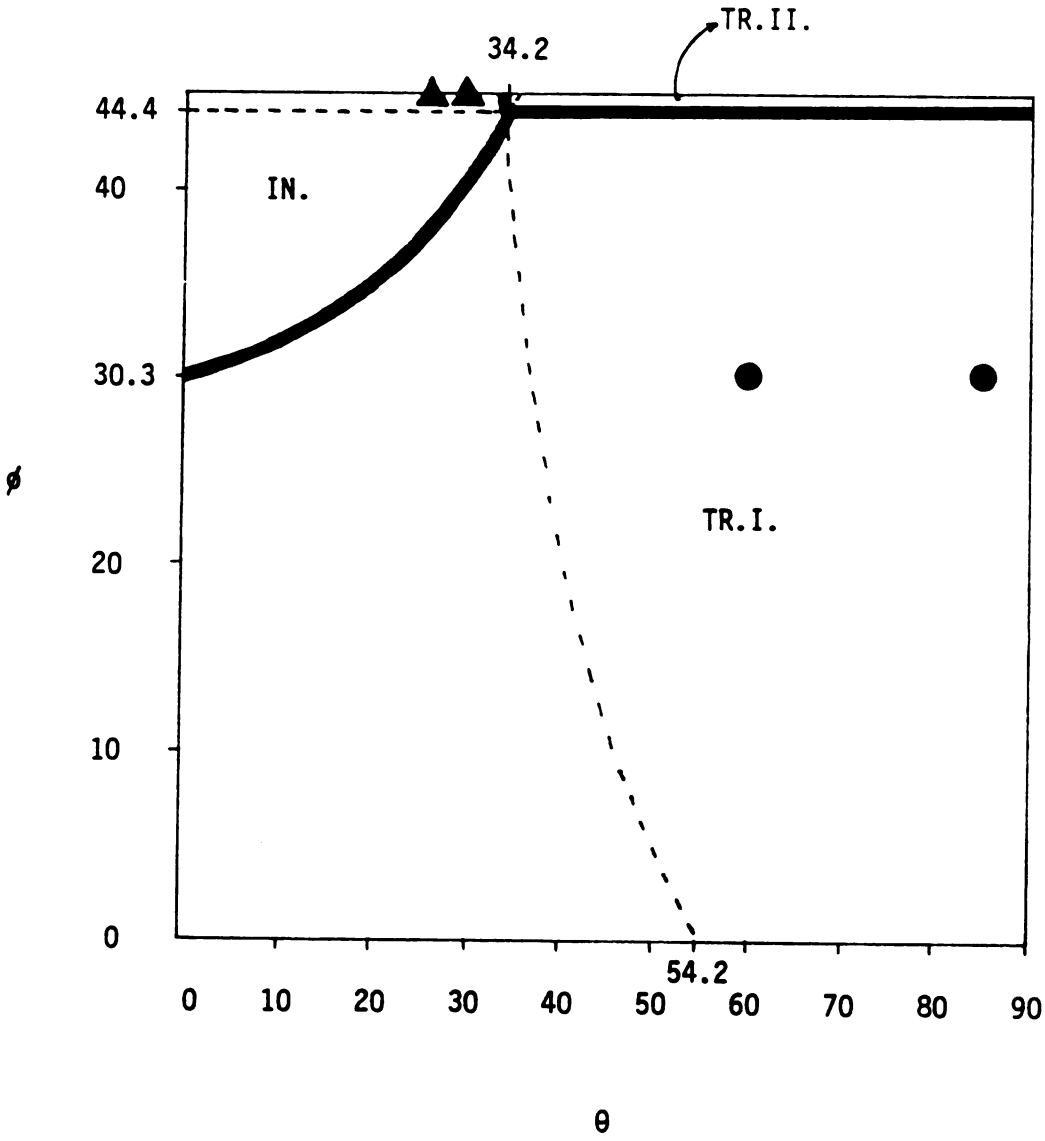
TR.II.
34.2
44.4
40
IN.
30.3
ϕ
TR.I.
20
10
0
54.2
0
10
20
30
40
50
60
70
80
90
θ

plane in grain II.

Experimental results are incorporated in this figure by placing different markers in order to indicate various fracture modes as a function of the misorientation angles θ and ϕ. As can be seen from the figure 36, the experimental observations fully conform with the predictions of the model. However, the number of results illustrating the propagation of (100) crack was quite a few because (100) crack initiation was very rare in the projectile velocity range (2.5 to 20 ms^{-1}) used in this research.

When the secondary cleavage crack is initiated and propagated in grain I along (110) plane, crack propagation conditions similar to those for the case of primary cleavage crack interaction with grain boundary exist as shown in figure 37. Under such conditions

$$\sigma_{(100)} = \sigma_g \cos^2 (45^o - \phi) \quad , \tag{52}$$

$$\sigma_{(110)} = \sigma_g \cos^2 \phi \quad , \text{ and} \tag{53}$$

$$\sigma_{gb} = \sigma_g \cos^2 \theta \quad . \tag{54}$$

From the equations (52), (54), and (43) the condition for transcrystalline crack propagation along the (010) cleavage plane instead of intercrystalline fracture is

$$\cos^2 (45^o - \phi) < 0.746 \cos^2 \theta \quad , \tag{55}$$

and the condition for intercrystalline fracture is

Figure 37. Schematic drawing of specimen surface illustrating potential crack propagation directions for the case of (110) crack interaction with grain boundary. Specimen surface is (001) in both grain.

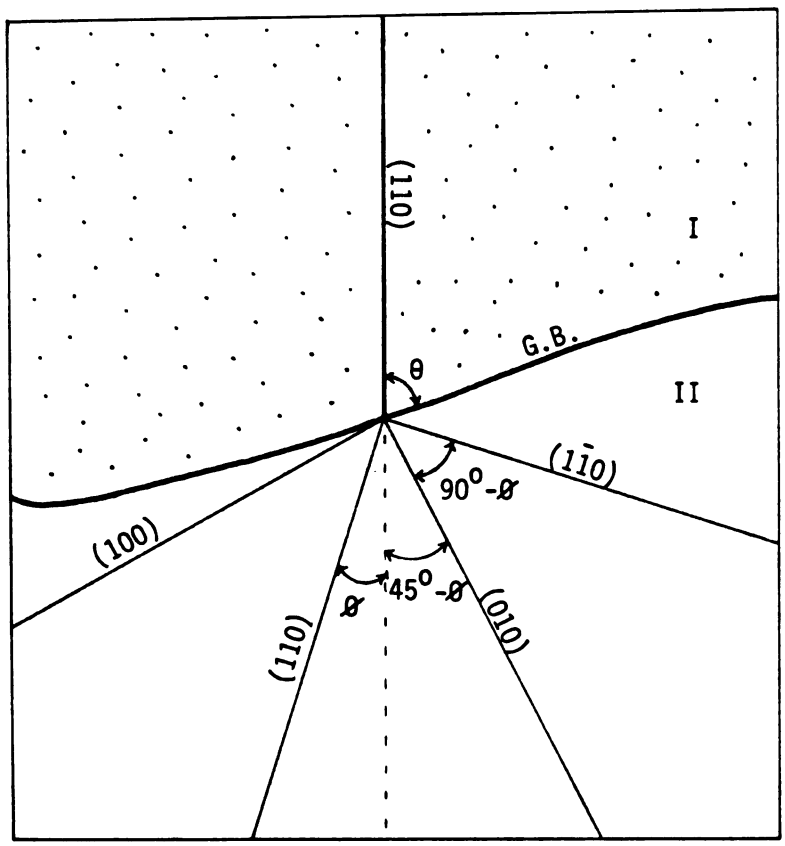
(110)
I
G.B.
θ
II
(1$\bar{1}$0)
90°-ø
(100)
ø
45°-ø
(110)
(010)

$$\cos^2 (45^o - \phi) > 0.746 \cos^2 \theta \quad . \tag{56}$$

Likewise, from the equations (53), (54), and (44), the condition for transcrystalline crack propagation along the (110) cleavage plane instead of intercrystalline fracture is

$$\cos^2 \phi < 1.461 \cos^2 \theta \quad . \tag{57}$$

From the equations (52), (53), and (45), the condition for crack propagation along the (010) cleavage plane instead of (110) cleavage in grain II is

$$\cos^2 (45^o - \phi) < 0.511 \cos^2 \phi \quad , \tag{58}$$

and the condition for intercrystalline fracture is

$$\cos^2 (45^o - \phi) > 0.511 \cos^2 \phi \quad . \tag{59}$$

These six conditions for the determination of crack path were drawn and superimposed in figure 38.

The three curves of figure 38 represent the various combinations of critical angles (θ and ϕ) that control the mode of crack propagation. The critical value of ϕ for the transcrystalline cleavage along the (010) or (110) planes is 0.6^o since the surface energy of (010) plane is much smaller than that of (110) plane. When the tilt angle (ϕ) is larger than 14.7^o, only primary cleavage fracture occurs regardless of the value of θ. For the values of θ ranging from 34.2^o to 90^o, primary cleavage always occurs provided ϕ is larger than 0.6^o. For the values of θ ranging from 0^o to 34.2^o, primary cleavage occurs provided ϕ is larger than the

Figure 38. Crack propagation mode for various ϕ and θ when (110) crack in grain I interacts with a tilt boundary (ϕ is tilt angle and θ is the angle between crack path in grain I and grain boundary).

● : Transcrystalline crack propagation along promary cleavage plane,

■ : Transcrystalline crack propagation along secondary cleavage plane,

▲ : Intercrystalline crack propagation,

IN. : Intercrystalline crack propagation zone,

TR.I.: Transcrystalline(primary) crack propagation zone, and

TR.II.: Transcrystalline(secondary) crack propagation zone.

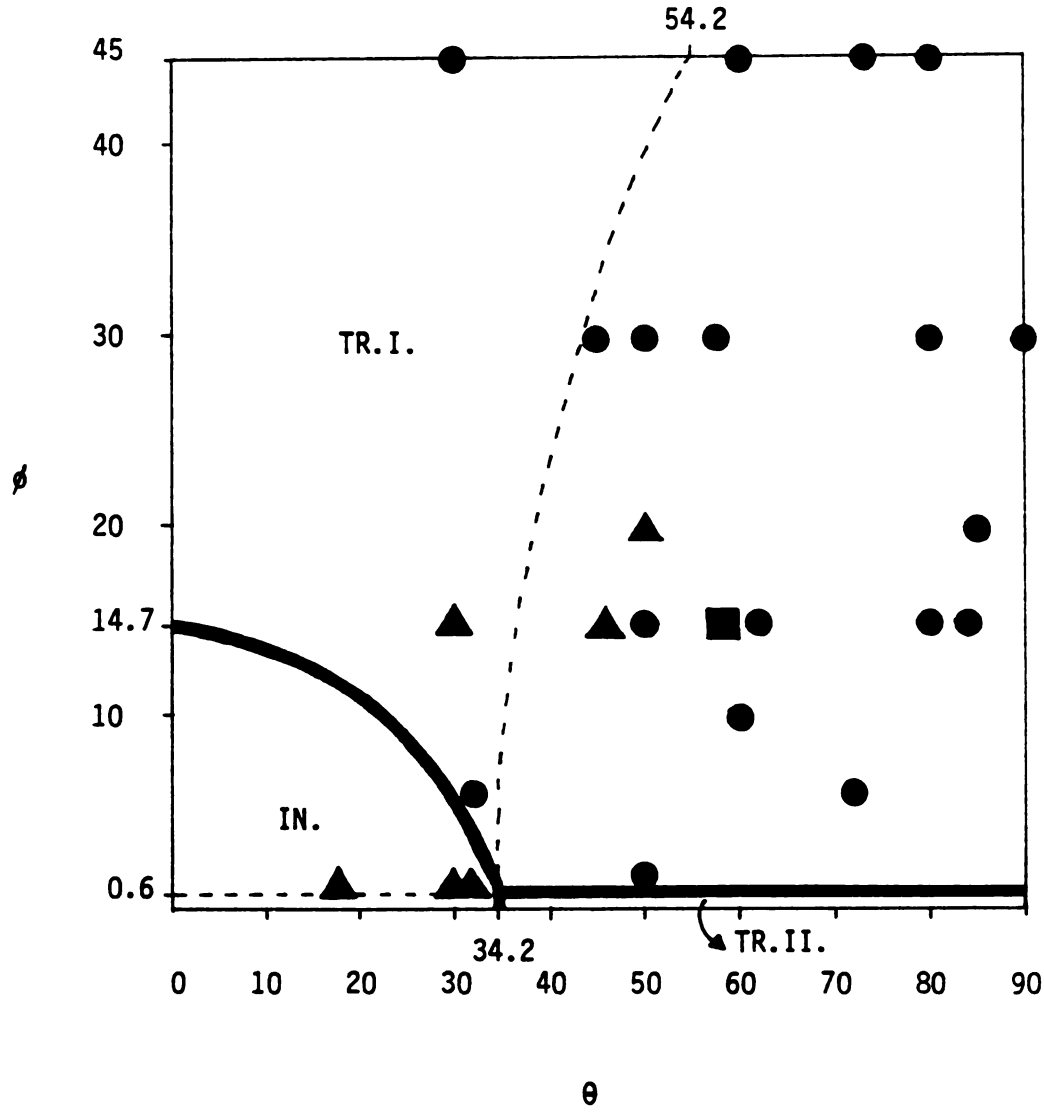
54.2
45
40
30
TR.I.
ϕ
20
14.7
10
IN.
0.6
34.2
TR.II.
0
10
20
30
40
50
60
70
80
90
θ

corresponding critical angles, ranging from 0.6^{o} to 14.7^{o}. For the case of (110) crack initiation, the domonant crack propagation mode is also transcrystalline crack propagation along the (010) primary cleavage plane in grain II because of the lower value of surface energy of (010) primary cleavage plane than that of the (110) secondary cleavage plane.

Experimental results are also incorporated in the figure 38. As can be seen in this figure, most of the experimental results conform with the prediction of the model. Such a good agreement is the same tendency as the case of mode I loading in the previous research.[71] This may imply that the direction of brittle crack propagation is mainly governed by the anisotropy of surface energy in crystals with strong cleavage tendencies regardless the crack initiation mechanism. Another possible reason for such a good agreement may be the similar magnitudes of the crack velocity. The velocity of cracks produced by particle impact in the present study is comparable with that obtained by mode I loading method since the range of projectile velocity used was very low (2.5 to 20 ms^{-1}).

However, four results do not match with the prediction of the model. For the case of two specimens (15^{o} and 20^{o} tilt), intercrystalline fractures and a secondary cleavage were observed in the zone which illustrates the angular conditions of the specimens for transcrystalline crack propagation along the primary cleavage plane in grain II. This mismatch may be due to the compromise between the crack propagation tendencies along the stress trajectory and cleavage planes. The stress distribution produced by dynamic loading near the grain boundary may be the another cause for such a mismatch between the experimental results and the prediction of the model. These experimental points that do not agree with the predictions of the model were observed to occur mainly when the point of impact was too close to the boundary. The complicated stress state

that will develop in the boundary region in such cases may be responsible for the inconsistencies observed.

4.1.2.4 Slip Propagation

The highly localized shear strain associated with slip in one grain of a LiF bicrystal introduces elastic or plastic distortion in the adjacent grain. One possible result is the generation of a crack when a slip band intercepts the grain boundaries having mixed characters. However, when the grain boundary has only pure tilt character, slip propagation can occur across the boundary if the dislocation pile-up stress reaches a critical value.

As can be seen in figure 39, usually very fine slip lines were formed under particle impact and they were usually blocked by the grain boundaries. This general tendency of the blockage of slip lines by grain boundaries implies that even the tilt boundaries are extremely effective barriers to the propagation of fine slip caused by particle impact. However, cracks caused by dislocation pile-up at the grain boundary have never been observed during this investigation. This implies that pile-up stresses are not high enough to cause crack nucleation based on the Stroh's model.

In some cases (figure 40), it was also observed that slip lines are continuous across the grain boundary showing slip propagation to the adjacent grains. Such slip propagation was also observed by Johnston et al[65] in MgO bicrystals having small tilt boundaries under compression. Furthermore, additional slip systems may also be found to be activated in adjacent grains as proposed by Cottrell[64] due to the stress concentration introduced by dislocation pile-up. These features are presented in figure 40. The continuity of slip across the boundary may imply that glide dislocations can

Figure 39. Blockage of slip lines (formed by particle impact) by a tilt boundary.

$\phi = 6^{o}$ $V = 20\ ms^{-1}$

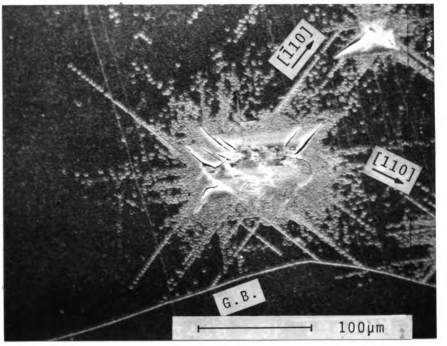
[110]
[110]
G.B.
100μm

Figure 40. Propagation of slip due to particle impact (near the grain boundary) through the grain boundary in regions marked 'X' and 'Y'.
(A). $\phi = 6^{o}$ $V = 5.5\ ms^{-1}$
(B). $\phi = 20^{o}$ $V = 11\ ms^{-1}$

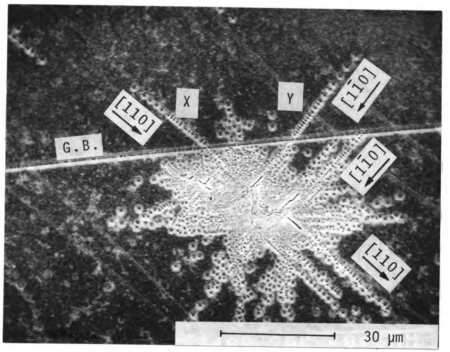

(A)

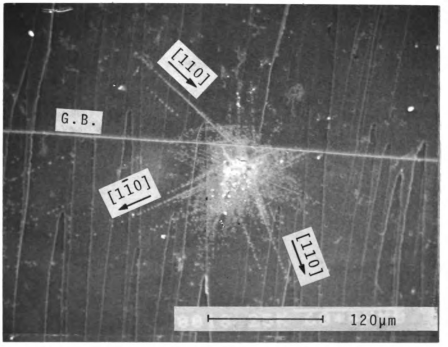

(B)

pass through the boundary as proposed by Marcincowski and Sadananda[66], and that the boundary itself may undergo deformation because of this passage. The results explaining such passage of dislocations were not obtained in this research since TEM could not be used for LiF due to its low melting point. The ease with which the boundary undergoes deformation should control the ease with which slip can propagate from one grain to the other. The slip propagation under particle impact occurred only when the misorientation angle is less than 20^{o}. This implies that the relative crystallographic orientation is an important factor that controls slip propagation through a grain boundary. The distance from the impact spot to the grain boundary is another important factor that determines when slip can propagate through a grain boundary. When the distance is less than the critical distance, most of the slip lines are blocked by the grain boundary as shown in figure 39.

When the particle impact occurred on the grain boundary, two sets of rosette patterns consisting of slip lines are observed in both grains as shown in figure 41. As can be seen in this figure, primary and secondary slip lines are formed in both grains independently due to the particle impact on the grain boundary.

4.2 Damage Produced by Quasi-static Indentation

As discussed in previous section 4.1.2.4, most of the fine slip lines formed by particle impact are blocked by the grain boundaries. On the other hand, indentation loading produces wide slip bands as shown in figure 42. The formation of such wide slip bands under indentation is mainly due to the much longer duration of loading time (about 10 seconds) compared with the very short loading time (few micro-seconds)[20] under particle impact. Under indentation, the rate of loading is also much slower

Figure 41. Rosette patterns formed by particle impact on the grain boundary.

(A). $\phi = 20^{o}$ $V = 2.5\ ms^{-1}$

(B). $\phi = 20^{o}$ $V = 16\ ms^{-1}$

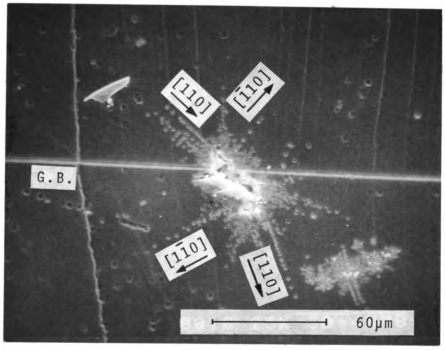

(A)

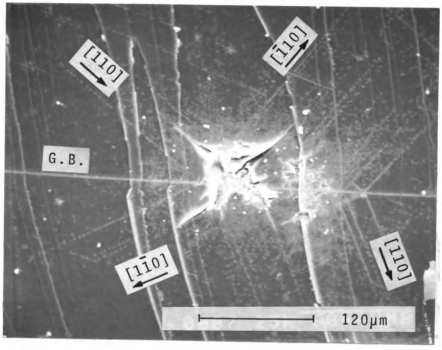

(B)

than the case of particle impact. Therefore, extensive plastic flow occurs with the formation of wide slip bands on the (001) surface of specimens under indentation.

Such wide slip bands are similar to the slip bands observed by Subramanian et al[77-79] in single crystals of rock-salt structure under compression or cyclic loading conditions. These wide slip bands propagate through the grain boundary easily when indentation is produced near the grain boundary as illustrated in figure 42 since the wide slip bands cause very effective pile-up stress on the boundary. This pile-up stress cause slip propagation instead of crack nucleation since boundary has tilt character only. Even though Johnston et al[65] concluded that the probability of crack nucleation by dislocation pile-up increases with increasing misorientation, no such cracks were observed in the LiF specimens having maximum tilt angle (45^{o}) during this investigation.

Due to the sharp tip of the pyramid indenter, the stress field produced by indentation corresponds to the Boussinesq type stress field. However, the equations describing Boussinesq stress field can not be used directly to the calculation of indentation stress in LiF bicrystals. As can be seen in equations (derived by Lawn and Swain[42]) which describe the stress components for the point loading in the range of elastic deformation, $\sigma_{er} = \sigma_{r\theta} = 0$. This stress component, σ_{er}, is the shear stress which causes slip along <110> directions. The crystal anisotropy also plays a very significant role as evidenced by the dislocation rosette pattern. Moreover, the specimens have strong anisotropic character possessing primary and secondary cleavage planes as well as primary and secondary slip systems just beneath the indentation site. In addition the indenter used was pyramidal, not conical.

Figure 42. Typical dislocation rosette pattern produced by the indentation in the grain boundary region.

$\phi = 6^{o}$ P = 0.245 N

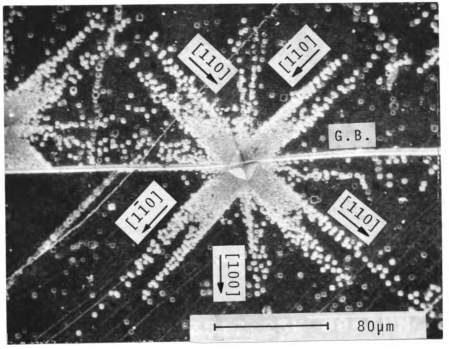
[110]
[1$\bar{1}$0]
G.B.
[1$\bar{1}$0]
[110]
[100]
80μm

The typical dislocation rosette pattern produced by indentation in the grain boundary region is shown in figure 42. Each etch pit corresponds to the intersection of a segment of a dislocation loop with the surface. Due to the cubic symmetry of LiF crystal, the rosette pattern consists of eight wings with lines of etch pits either in the <100> direction or in the <110> direction. This rosette pattern is very similar to that obtained by Armstrong and Wu[63] in MgO single crystals with pyramid indentation method as shown in figure 7. And the etch pit patterns observed in indentation test are very similar to those produced by particle impact in LiF bicrystals, although the extent of deformation and width of the slip bands differed in both cases. Such similarity was also observed by Evans and Wilshaw[18] in ZnS under fully plastic contact conditions.

When the indenter elastically contacts the LiF crystal, resolved shear stresses are developed on the $\{110\}_{45}o$ planes but not on the $\{110\}_{90}o$ planes.[60] These stresses on the $\{110\}_{45}o$ planes nucleate new dislocations and cause slip. After the indenter penetrates into the crystal, shear stresses develop on the $\{110\}_{90}o$ planes also.[60] The insertion of the pyramidal indenter into a (001) surface of LiF crystal displaces material along the <110> slip directions forming two rows of edge dislocations.[61] The dislocation loops formed on $\{110\}_{45}o$ and $\{110\}_{90}o$ planes are shown schematically in figure 6. Etch pits due to edge dislocations extend along the <110> directions while those due to screw dislocations extend along the <100> directions as observed by Keh[60] and Vaughan et al.[61] The dislocations formed on the two sides of each wing are of opposite sign because they are formed by a shear stress which is introduced by the indentation process, during which the material is pushed away by the indenter.[60]

Dislocations pile-up on slip planes at barriers such as grain boundaries, second phases, or sessile dislocations. Most pile-ups are made up of dislocations with an edge component since screw dislocations can cross-slip out of the slip plane. In the present study, edge dislocation pile-ups at grain boundaries are observed and analyzed according to the nature of specimens and loading conditions. The distribution of dislocations in a pile-up has been calculated by Eshelby et al[80]. The number of edge dislocations (N) along a slip plane between the indentation and grain boundary is[80]

$$N = \frac{(1-\nu)\, D\tau_s}{Gb} \quad . \tag{60}$$

where, D is distance of indentation from the grain boundary,

τ_s is average resolved shear stress in the slip plane,

G is shear modulus of specimen, and

b is magnitude of Burgers vector.

The leading edge dislocation in the pile-up is acted on by the interaction force with other dislocations as well as the applied shear stress which induce a high stress concentration on the leading dislocation in the pile-up. The magnitude of this pile-up stress is proportional to the applied shear stress, and this shear stress in the boundary region decreases as the indentation distance from the grain boundary increases. When the pile-up contains many dislocations, the large stresses that develop can either nucleate a crack at the boundary, or initiate slip in the adjacent grain.[16] Pile-ups form until the force on the leading dislocations is sufficient to make them break through the grain boundary.

According to Stroh's model[73], crack froms when the leading dislocations in a pile-up are forced to within a distance 'b' of one another. Stokes et al[81] observed such cracks in a MgO single crystals under compression. In the LiF bicrystals with pure tilt character, there are two potential slip planes in grain II, and these two planes have the same zone axis as the slip plane containing dislocation pile-ups in grain I. Under such conditions, the slip lines can propagate easily to the adjacent grain without forming any Stroh type crack. The magnitude of the stress level needed for slip propagation is less than that needed for crack initiation in LiF bicrystals.

The dislocation rosette patterns produced by indentation loading are analyzed in terms of indentation load, misorientation angle, and the indentation distance from the grain boundary. According to the definition of Vickers hardness (Hv), indentation load (P) is related to the diagonal length of indentation (D_c) by the following equation.[82]

$$Hv = \frac{2P \sin 136^{o}/2}{D_c^{2}} \quad . \tag{61}$$

This parabolic relation between the indentation load and the diagonal length of indentation is shown in figure 43.

The size of rosette pattern can be determined by the average distance over which the leading edge dislocations extend. The distance of travel of leading edge dislocations increases as the diagonal length of indentation increases, as illustrated in figure 44. Such tendency between indentation load and crack length was also observed by Palmqvist[41] in carbides.

Figure 43. The relation between indentation load and the diagonal length of indentation.

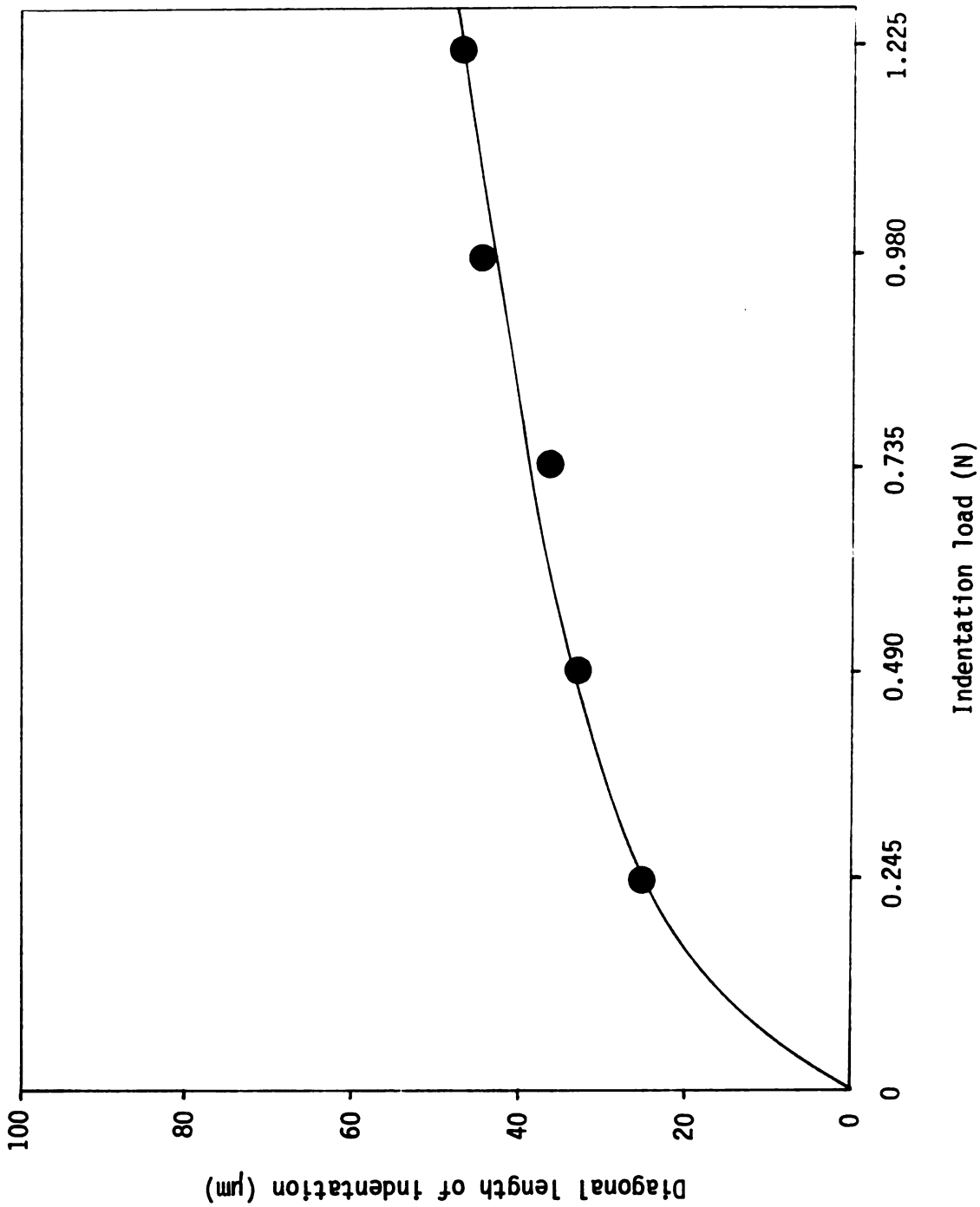
Diagonal length of indentation (μm)
100
80
60
40
20
0
0
0.245
0.490
0.735
0.980
1.225
Indentation load (N)

Figure 44. Plot of diagonal length of indentation versus the distance of travel of leading edge dislocation.

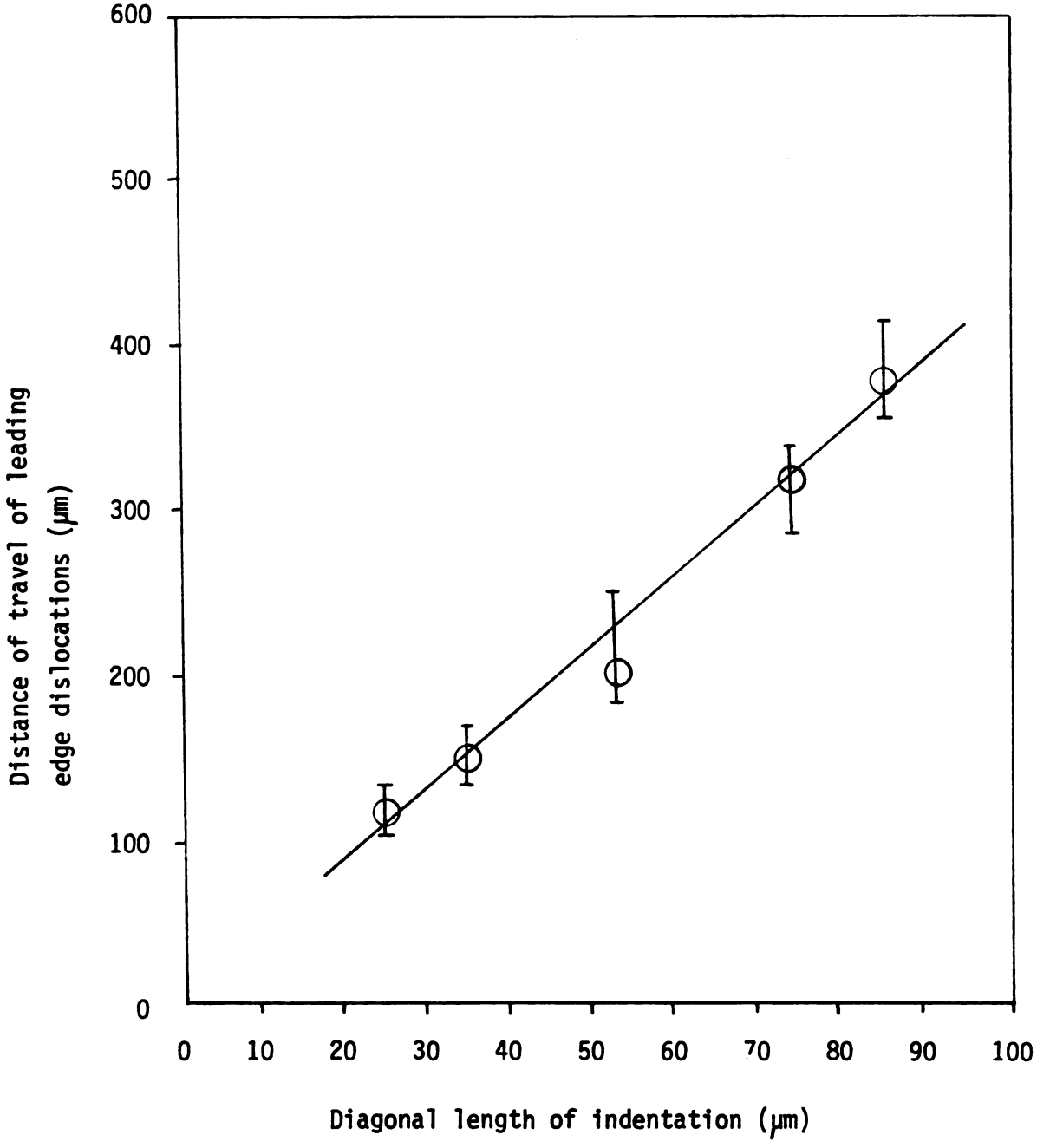
600
500
400
300
200
100
0
0
10
20
30
40
50
60
70
80
90
100
Distance of travel of leading edge dislocations (μm)
Diagonal length of indentation (μm)

The distance between the grain boundary and the indentation site is an important factor in slip propagation mechanism since the stress concentration at grain boundary due to indentation decreases as this distance increases. As can be seen in figure 45(A), dislocations pile-up at grain boundary when the distance between indentation and grain boundary is shorter than the distance of travel of leading edge dislocation. The maximum number of piled-up dislocations are observed when indentation distance equals the critical distance at which slip propagation to the adjacent grain just initiates. On the other hand, dislocations resulting from indentation at a distance shorter than the critical distance propagate across tilt boundaries as shown in figure 45 (A) and (B). After propagating across the tilt boundary, slip lines bend to comply with the misorientation between the adjacent grains as can be seen in figure 45(B). These slip bands are very wide compared with the fine slip lines produced by particle impact, and as a result are capable of producing higher stress concentration at the boundary.

The relation between the indentation distance and the length of slip lines in the adjacent grain is plotted in figure 46. As can be seen in this graph, the length of propagated slip lines decreases as the indentation distance increases. The intersecting points of each curve with abscissa (corresponding to zero propagation length of slip line in adjacent grain) gives the corresponding critical indentation distances for the three misorientation angles. The propagated slip line length also decreases as the misorientation angle increases.

Relative crystallographic misorientation also has a strong influence on the slip propagation mechanism. Misorientation angle of each bicrystal was determined by measuring the misfit angle between two slip lines formed

Figure 45. Dislocation pile-up and slip propagation through tilt boundary under indentation loading.

(A). $\phi = 6^{o}$ P = 0.245 N

(B). $\phi = 10^{o}$ P = 0.490 N

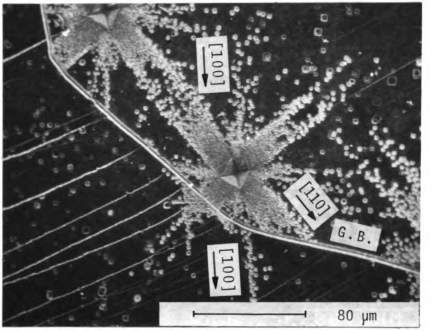

(A)

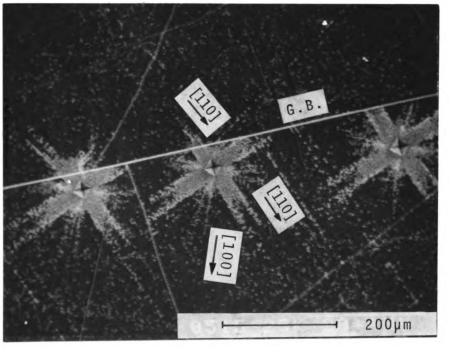

(B)

Figure 46. Plot of distance between the grain boundary and indentation site versus slip line length in adjacent grain (grain II).

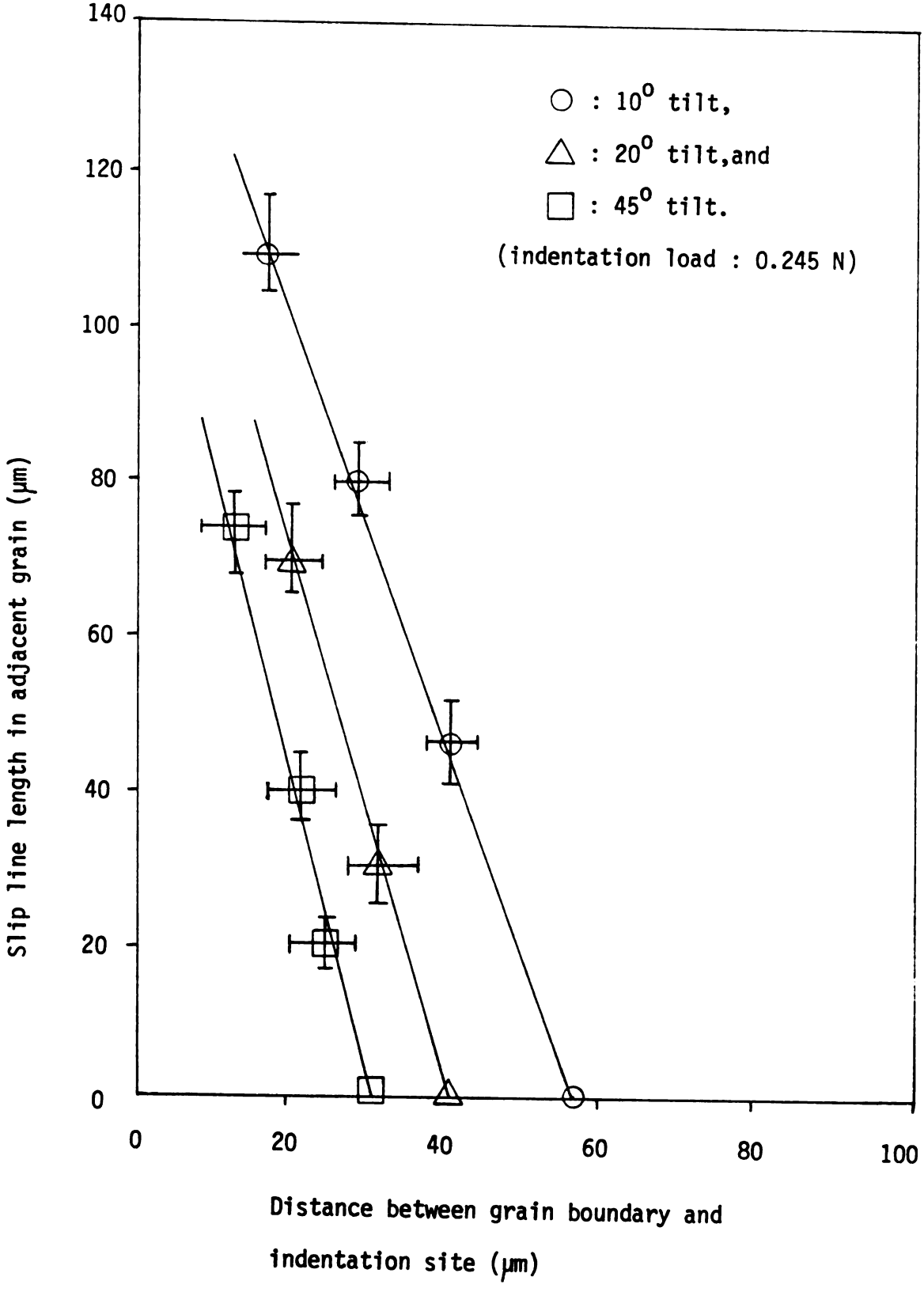
140
120
100
80
60
40
20
0
0
20
40
60
80
100
○ : 10° tilt,
△ : 20° tilt,and
□ : 45° tilt.
(indentation load : 0.245 N)
Slip line length in adjacent grain (μm)
Distance between grain boundary and
indentation site (μm)

along the primary slip directions of both grains. The slip propagation through grain boundary has been usually observed when 90^{o} slip bands in grain I interact with the boundary. This may be due to effective pile-up of stress that can develop when edge dislocations are blocked by the boundary. In the case of 45^{o} slip band intersecting with the boundary, screw dislocations present in such slip bands may cross-slip to relieve pile-up stress. The relation between the misorientation angle and the corresponding critical indentation distance is shown in figure 47. Due to the geometrical relationship between two primary slip planes of grain I and II, resolved shear stress on the primary slip plane of grain II decreases as the misorientation angle increases. This may be due to the fact that the resolved shear stress in a given slip plane of grain II depends on the misorientation angle. Therefore, the critical distance for slip propagation decreases as the misorientation angle increases as can be seen in figure 47.

Indentation load is also an important factor in the slip propagation mechanism. In the stress field produced by pyramid indenter, the stress concentration at grain boundary increases as the indentation load is increased. This tendency can be seen in the plot provided in figure 48, for a specimen with 15^{o} tilt boundary.

By superimposing the tendencies revealed in the two figures 47 and 48 illustrating the change of critical indentation distance on the different values of tilt angle and indentation load, the conditions for the propagation of slip lines in LiF bicrystals possessing pure tilt character is essentially established.

When pyramid indentations were made on a cleaved surfaces of a LiF bicrystals using loads ranging from 0.245 to 5.145 N, cracks on the

Figure 47. Plot of misorientation angle versus critical indentation distance for slip propagation.

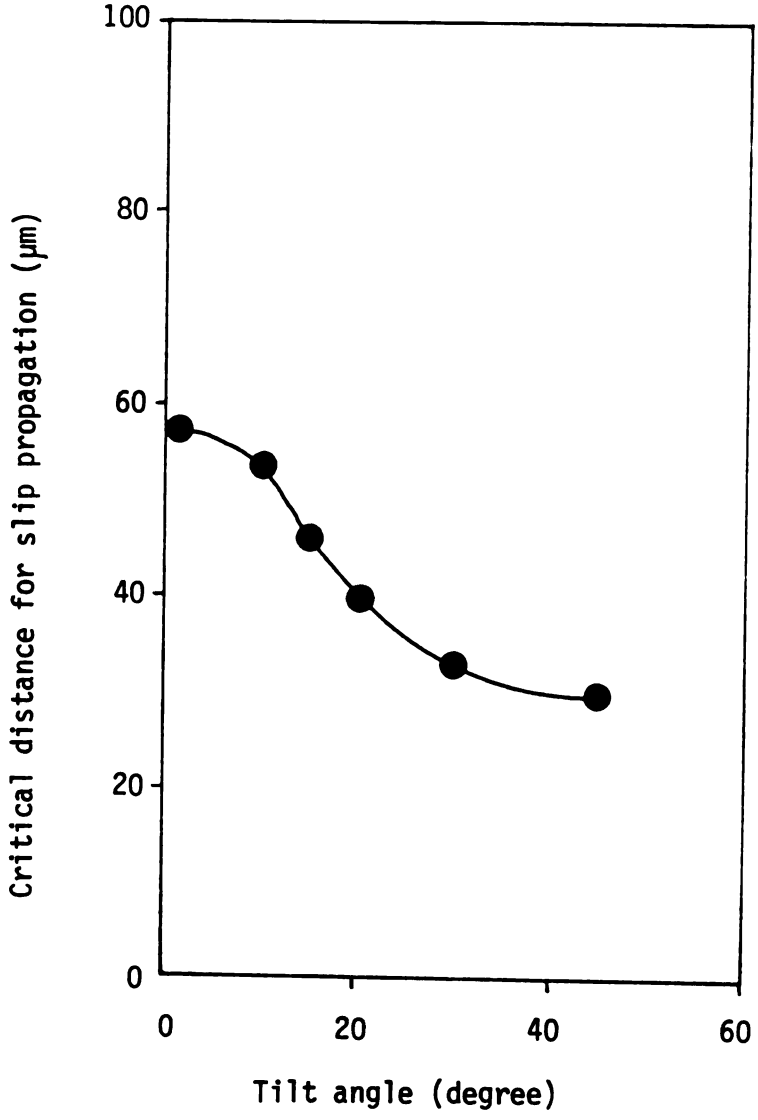
100
80
60
40
20
0
0
20
40
60
Critical distance for slip propagation (μm)
Tilt angle (degree)

Figure 48. Plot of indentation load versus the critical indentation distance for slip propagation.

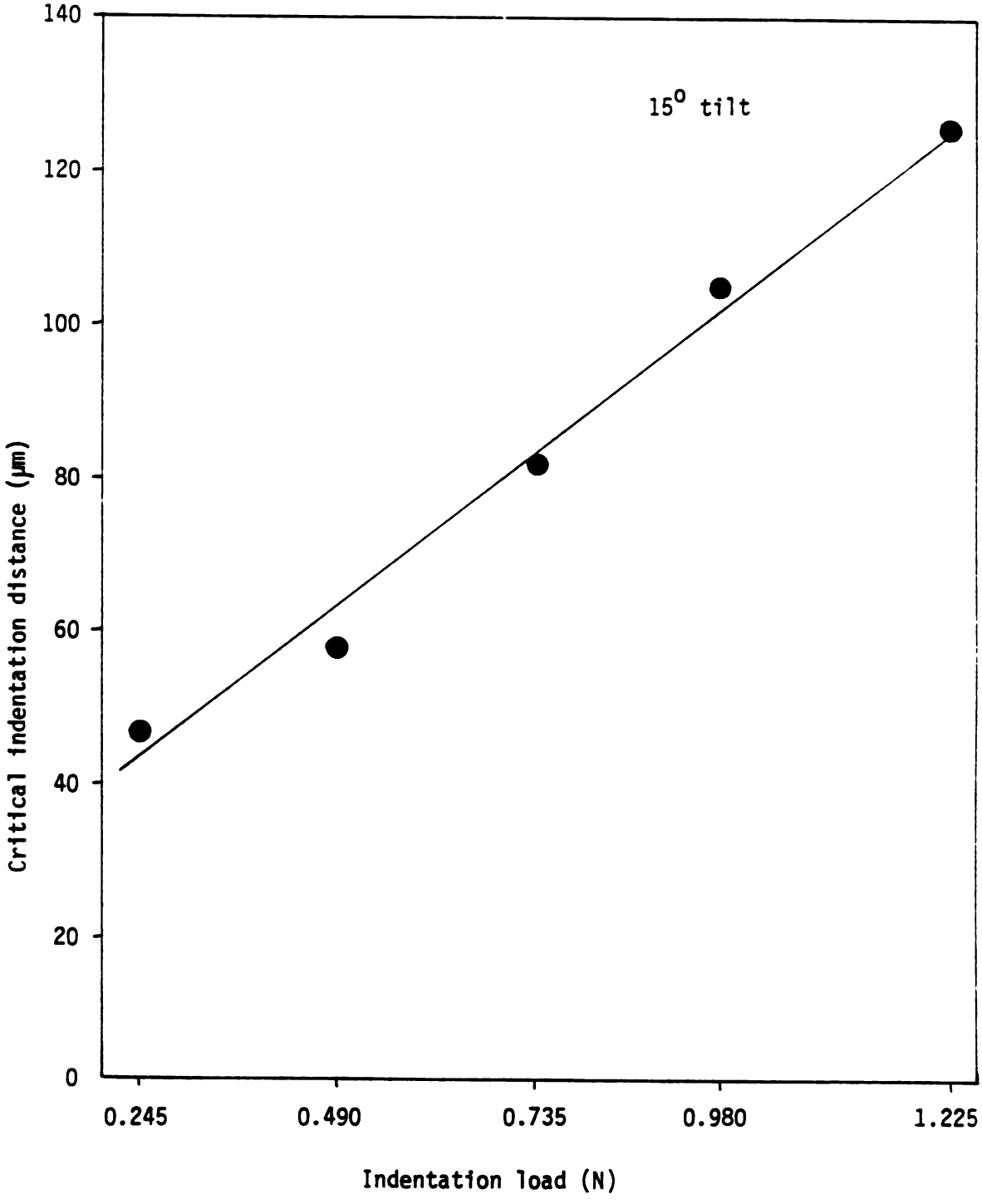
140
120
100
80
60
40
20
0
15° tilt
Critical indentation distance (μm)
0.245
0.490
0.735
0.980
1.225
Indentation load (N)

specimen surface were never observed due to the slow loading rate and ductility of LiF under such conditions. Petrovic and Mendiratta[55] observed sharp cracks initiated from the corners of the pyramid indentation. In the case of indentation on MgO single crystals with few grams load, cracks were formed in the <110> direction due to its lower ductility as compared with LiF.[60] By chemical polishing method, Keh found that those cracks lay in the $\{110\}_{90}$° planes. Keh et al[60] observed the same type cracks in LiF single crystals when the indentation was carried out at a sub-zero temperature. Hagan[62] has observed only sub-surface cracks beneath the indented surface under similar loading conditions to those used in the present research. The direction of such cracks is exactly same as the crack directions observed in the LiF specimens under impact erosion.

As discussed in the previous sections 4.1.1.1 and 4.1.2.1, lateral fractures are the main features of the surface damage under impact erosion in LiF crystals. Such lateral fractures were also observed even at very low projectile velocities (about 2.5 ms^{-1}). However, under indentation test of LiF crystals carried out at room temperature, lateral fractures were never observed. Such observations imply that the loading rate and ductility of material are the main contributing factors for material removal mechanism since the main source of material removal under impact erosion is the intersection of lateral fracture with another lateral fracture or grain boundaries. Observations of such a fine slip due to particle impact, and formation of wide slip bands under indentation loading, also emphasize the importance of rate of loading in deformation of semi-brittle materials.

V. CONCLUSIONS

The fracture and deformation of bicrystals of LiF, a semi-brittle material, under particle impact erosion and quasi-static indentation were investigated experimentally. The main conclusions obtained during this investigation are as follows:

1. In crystals with strong cleavage tendencies, like LiF, there is some compromise between the tendencies for cracks to follow stress trajectories and cleavage planes.

2. Particle impact of LiF crystal causes (110) cracks initiated predominantly according to Keh's model. Under indentation loading at room temperature, using loads ranging from 0.245 to 5.145 N, lateral fractures were never observed, whereas they were the main features of surface damage under impact erosion in LiF crystals. This implies that the loading rate and ductility of materials play significant roles in material removal mechanism in impact erosion.

3. When the cracks due to the particle impact reach the grain boundary present in a bicrystal, they initiate intercrystalline or trans-crystalline cracks provided they are not blocked by the grain boundaries due to large crystallographic misorientations between the adjacent grains or due to a weak driving force for crack propagation resulting from large distances of impact from the boundary.

4. Experimental results on crack propagation in the grain boundary region under particle impact are in good agreement with the

predictions of a model for mode I crack propagation based on the normal stress law for brittle fracture. This implies that the crack propagation direction in crystals with strong cleavage tendencies is mainly governed by the anisotropy of surface energy even under impact loading conditions.

5. The main cause of material removal in LiF single crystals under particle impact using blunt projectiles is the interaction of lateral fracture. However, under this condition, material removal from bicrystals occurs by interaction of lateral fractures with other lateral fractures or grain boundaries.

6. Fine slip occurs as a result of particle impact, and such fine slip is usually blocked by the grain boundary. Slip propagation through the grain boundary was rarely observed under such conditions. On the other hand, under indentation loading, wide slip bands are formed. When such wide slip bands interact with tilt boundary, slip propagation through the boundary usually occurs. This may be due to more effective stress concentration that may arise when wide slip band is blocked by the boundary. However, presence of applied load for sufficient lengths of time during indentation may also aid this process.

7. The main factors having strong influence on the slip propagation mechanism under indentation loading are indentation distance from the grain boundary, relative crystallographic misorientation, and magnitude of indentation load. The critical indentation distance for slip propagation decreases as the relative crystallographic misorientation angle between the grains increases.

8. Dislocation pile-ups at pure tilt boundaries in LiF bicrystals do not cause enough stress cencentrations to initiate crack. Crack nucleation caused by the blockage of slip at tilt boundaries was not observed, either under particle impact or under indentation loading. The observations of slip propagation to the adjacent grain during quasi-static indentations imply that the magnitude of stress concentration needed for crack initiation is larger than that needed for slip propagation through simple tilt boundaries of LiF bicrystals.

9. In a semi-brittle material like LiF, deformation and fracture caused by quasi-static indentation produced by Vickers hardness test are not representative of damage resulting from low velocity (up to 20 ms^{-1}) particle impact.

Bibliography

1. F.B. Langitan and B.R. Lawn, "Hertzian Fracture Experiments on Abraded Glass Surfaces as Definitive Evidence for an Energy Balance Explanation of Auerbach's Law," J. Appl. Physics, 40, 4009 (1969).

2. F.B. Langitan and B.R. Lawn, "Effect of a Reactive Environment on the Hertzian Strength of Brittle Solids," J. Appl. Physics, 42, 5540 (1971).

3. G.P. Tilly, "A Two Stage Mechanism of Ductile Erosion," Wear, 23, 87 (1973).

4. S.M. Wiederhorn and D.E. Roberts, "A Technique to Investigate High Temperature Erosion of Refractories," Am. Ceram. Soc. Bull., 55, 185 (1976).

5. S.M. Wiederhorn and B.R. Lawn, "Strength Degradation of Glass Impacted with Sharp Particles: I, Annealed Surfaces," J. Am. Ceram. Soc., 62, 66 (1979).

6. B.R. Lawn and D.B. Marshall, "Strength Degradation of Glass Impacted with Sharp Particles: II, Tempered Surfaces," J. Am. Ceram. Soc., 62, 71 (1979).

7. D.B. Marshall and A.G. Evans, "Measurement of Dynamic Hardness by Controlled Sharp-Projectile Impact," J. Am. Ceram. Soc., 66, 580 (1983).

8. I. Finnie, "Erosion of Surfaces by Solid Particles," Wear, 3, 87 (1960).

9. A.G. Evans, "Strength Degradation by Projectile Impacts," J. Am. Ceram. Soc., 56, 405 (1973).

10. R.E. Winter and I.M. Hutchings, "Similarities and Differences in the Erosion Behavior of Materials," Wear, 25, 141 (1975).

11. S.M. Wiederhorn and B.R. Lawn, "Strength Degradation of Glass Resulting from Impact with Spheres," J. Am. Ceram. Soc., 60, 451 (1977).

12. F.F. Lange and A.G. Evans, "Erosive Damage Depth in Ceramics: A study on Metastable, Tetragonal Zircornia," J. Am. Ceram. Soc., 62, 62 (1979).

13. C.E. Smeltzer, M.E. Gulden, and W.A. Compton, "Mechanisms of Metal Removal by Impacting Dust Particles," J. Basic Eng., Trans. ASME, 92D, 639 (1970).

14. M.E. Gulden, "Effect of Number of Impacts on Erosion of Polycrystalline MgF_2 in the Elastic-Plastic Response Regime," J. Am. Ceram. Soc., 63, 121 (1980).

15. J.R. Lewis, "Erosion Characteristics of Materials for Centrifugal Coal Slurry Pumps, Presentation TMS-AIME Meeting (1984), Abstract in J. of Metals, p. 55, July (1984).

16. J.P. Hirth and J. Lothe, Theory of Dislocations, P. 377, McGraw-Hill Book Co., New York, 1968.

17. J. Washburn, G.W. Groves, A. Kelly, and G.K. Williamson, "Electron Microscope Observations of Deformed Magnesium Oxide," Phil. Mag., 5, 991 (1960).

18. A.G. Evans and T.R. Wilshaw, "Dynamic Solid Particle Damage in Brittle Materials," J. Mater. Sci., 12, 97 (1977).

19. J.E. Ritter, P. Strzepa, K. Jakus, L. Rosenfeld, and K.J. Buckman, "Erosion Damage in Glass and Alumina," J. Am. Ceram. Soc., 67, 769 (1984).

20. C.G. Knight, M.V. Swain, and M.M. Chaudhri, "Impact of Small Steel Spheres on Glass Surfaces," J. Mater. Sci., 12, 1573 (1977).

21. S. Timoshenko and J.N. Goodier, Theory of Elasticity, p. 383, McGraw-Hill Book Co., New York, 1951.

22. D.G. Rickerby, B.N. Pramilabai, and N.H. Macmillan, "The Influence of Particle Properties on Impact Damage in LiF," J. Mater. Sci., 14, 3006 (1979).

23. D. Tabor, The Hardness of Metals, p. 120, Clarendon Press, Oxford, 1951.

24. S.M. Wiederhorn and B.J. Hockey, "Effect of Material Parameters on

the Erosion Resistance of Brittle Materials," J. Mater. Sci., 18, 305 (1983).

25. G.L. Sheldon, "Similarities and Differences in the Erosion Behavior of Materials," J. Basic Eng., Trans. ASME, 62D, 619 (1970).

26. G. Hoff, W. Herbert, and H. Rieger, "Rain and Sand Erosion, Phenomena of Material Destruction Caused by Repeated Loads," Characterization and Determination of Erosion Resistance, ASTM Spec. Tech. Publ., No. 474, p. 353 (1970).

27. M.M. Chaudhri, J.K. Wells, and A. Stephens, "Dynamic Hardness, Deformation and Fracture of Simple Ionic Crystals at Very High Rates of Strain," Phil. Mag., 43, 643 (1981).

28. I.M. Hutchings, "Energy Absorbed by Elastic Waves during Plastic Impact," J. Phys. D., Appl. Phys. 12, 1819 (1979).

29. J.P. Ashford, Special Ceramics 4, Published by British Ceramic Research Association, pp. 173-189 (1969).

30. M.M. Chaudhri and P.A. Brophy, "Single Particle Impact Damage of Fused Silica," J. Mater. Sci., 15, 345 (1980).

31. R.H. Marion, "Use of Indentation Fracture to Determine Fracture Toughness," Fracture Mechanics Applied to Brittle Materials, ASTM Spec. Tech. Publ., No. 678, p. 103 (1978).

32. J.J. Gilman, "Hardness of Pure Alkali Halides," J. Appl. Phys., 44, 982 (1973).

33. D.R. Pande and T.S. Murty, "Mechanism for the Formation of {100} Slip Lines around a Dynamical Indentation on 100 Faces of Sodium Chloride Single Crystals," J. Phys. D., 7, 403 (1974).

34. B.R. Lawn, S.M. Wiederhorn, and H.H. Johnson, "Strength Degradation of Brittle Surfaces: Blunt Indenters," J. Am. Ceram. Soc., 58, 428 (1975).

35. B.R. Lawn, E.R. Fuller, and S.M. Wiederhorn, "Strength Degradation of Brittle Surfaces: Sharp Indenters," J. Am. Ceram. Soc., 59, 193 (1976).

36. B.R. Lawn and D.B. Marshall, "Hardness, Toughness, and Brittleness:

An Indentation Analysis," J. Ceram. Soc., 62, 347 (1979).

37. J.T. Hagan, "Shear Deformation under Pyramidal Indentations in Soda-lime Glass," J. Mater. Sci., 15, 1417 (1980).

38. J.C. Conway, Jr. and H.P. Kirchner, "The Mechanics of Crack Initiation and Propagation beneath a Moving Sharp Indenter," J. Mater. Sci., 15, 2879 (1980).

39. B.R. Lawn, T.P. Dabbs, and C.J. Fairbanks, "Kinetics of Shear-Activated Indentation Crack Initiation in Soda-lime Glass," J. Mater. Sci., 18, 2785 (1983).

40. D.B. Marshall, "Geometrical Effects in Elastic/Plastic Indentation," J. Am. Ceram. Soc., 67, 57 (1984).

41. B.R. Lawn and R. Wilshaw, "Review, Indentation Fracture: Principles and Applications," J. Mater. Sci., 10, 1049 (1975).

42. B.R. Lawn and M.V. Swain, "Microfracture beneath Point Indentations in Brittle Solids," J. Mater. Sci., 10, 113 (1975).

43. J.T. Hagan and M.V. Swain, "The Origin of Median and Lateral Cracks around Plastic Indents in Brittle Materials," J. Phys. D. Appl. Phys. 11, 2091 (1978).

44. A.H. Cottrell, "Theory of Brittle Fracture in Steel and Similar Metals," Trans. Met. Soc. AIME 212, 192 (1958).

45. A.S. Keh, J.C.M. Li, and Y.T. Chou, "Cracks due to the Pilling-up of Dislocations on Two Intersecting Slip Planes in MgO Crystals," Acta Metall., 1, 694 (1959).

46. B.R. Lawn and A.G. Evans, "A Model for Crack Initiation in Elastic/Plastic Indentation Fields," J. Mater. Sci., 12, 2195 (1977).

47. S. Palmqvist, Archiv Eisenhüttenwesen, 33, 629 (1962), as cited in Fracture Mechanics Applied to Brittle Materials, ASTM Spec. Tech. Publ., No. 678, p. 112 (1978).

48. V.W. Dawihl and G. Altmeyer, Zeitschrift für Metallkunde, 55, 231 (1964), as cited in Fracture Mechanics Applied to Brittle Materials, ASTM Spec. Tech. Publ., No. 678, p. 114 (1978).

49. B.R. Lawn and E.R. Fuller, "Equilibrium Penny-like Cracks in

Indentation Fracture," J. Mater. Sci., 10, 2016 (1975).

50. A.G. Evans, "Fracture Toughness: The Role of Indentation Techniques," Fracture Mechanics Applied to Brittle Materials, ASTM Spec. Tech. Publ., No. 678, p. 113 (1978).

51. J.J. Petrovic and M.G. Mendiratta, "Fracture from Controlled Surface Flaws," Fracture Mechanics Applied to Brittle Materials, ASTM Spec. Tech. Publ., No. 678, p. 83 (1978).

52. J.T. Hagan, "Cone Cracks around Vickers Indentations in Fused Silica Glass," J. Mater. Sci., 14, 462 (1979).

53. B.R. Lawn, "Hertzian Fracture in Single Crystals with the Diamond Structure," J. Appl. Physics, 39, 4828 (1968).

54. J.L. Routbort, R.O. Scattergood, and E.W. Kay, "Erosion of Silicon Single Crystals," J. Am. Ceram. Soc., 63, 635 (1980).

55. S.R. Schuon, "Microstructural Aspects of Impact Erosion in Lif, NaCl, KCl, and CaF_2 Single Crystals," Ph.D. Thesis, Michigan State University, East Lansing, Mi, 1980.

56. S.R. Schuon and K.N. Subramanian, "Impact Erosion of Single Crystals of LiF and CaF_2 by Sharp Projectiles," Wear, 81, 357 (1982).

57. S.R. Schuon and K.N. Subramanian, "Microstructural Aspects of Impact Erosion in Single Crystals of Lif, NaCl, KCl and CaF_2 by Blunt Projectiles," J. Mater. Sci., 18, 732 (1983).

58. I. Finnie, "Some Observations on the Erosion of Ductile Metals," Wear, 19, 81 (1972).

59. E. Aerts, S. Amelinckx, and W. Dekeyser, "The Surface Hardening of X-ray Irradiated NaCl," Acta Metall., 7, 29 (1959).

60. A.S. Keh, "Dislocations in Indented Magnesium Oxide Crystals," J. Appl. Physics, 31, 1538 (1960).

61. W.H. Vaughan and J.W. Davisson, "Dislocation Motion Associated with Indentations," Acta Metall., 6, 554 (1958).

62. J.T. Hagan, "Micromechanics of Crack Nucleation during Indentations," J. Mater. Sci. 14, 2975 (1979).

63. R.W. Armstrong and C.C.M. Wu, "Lattice Misorientation and Displaced

Volume for Microhardness Indentations in MgO Crystals," J. Am. Ceram. Soc., 61, 102 (1978).

64. A.H. Cottrell, Dislocation and Plastic Flow in Crystals, p. 107, Clarendon Press, Oxford, 1953.

65. T.L. Johnston, R.J. Stokes, and C.H. Li "Crack Nucleation in Magnesium Oxide Bicrystals under Compression," Phil. Mag., 7, 23 (1962).

66. K. Sadananda and M.J. Marcinkowski, "Deformation of Internal Boundaries," J. Mater. Sci., 9, 245 (1974).

67. F.F. Lange, "Mathematical Characterization of a General Bicrystal," Acta Metall., 15, 311 (1967).

68. A.R.C. Westwood, "On the Fracture Behavior of Magnesium Oxide Bicrystals," Phil. Mag., 6, 195 (1961).

69. R.D. Carnahan, T.L. Johnston, R.J. Stokes, and C.H. Li, "Effect of Grain Size on the Deformation of Polycrystalline Silver Chloride at Various Temperatures," Trans. AIME, 221, 45 (1961).

70. T.L. Johnston, C.H. Li, and R.J. Stokes, "The Strength of Ionic Solids," Strengthening Mechanisms in Solids, p. 341, ASM, Metals Park, OH (1962).

71. J.Y. Lee and K.N. Subramanian, "Fracture of LiF Bicrystals," J. Mater. Sci., 18, 1765 (1983).

72. A.W. Ruff and L.K. Ives, "Measurement of Solid Particle Velocity in Erosive Wear," Wear, 35, 195 (1975).

73. A.N. Stroh, "The Formation of Cracks in Plastic Flow. II," Proc. Roy. Soc. London, A 232, 548 (1955).

74. J. Washburn, A.E. Gorum, and E.R. Parker, "Cause of Cleavage Fractures in Ductile Materials," Trans. AIME, 215, 230 (1959).

75. F.C. Frank and B.R. Lawn, "On the Theory of Hertzian Fracture," Proc. Roy. Soc. London, A 299, 291 (1967).

76. L. Sohncke, Poggendorfs Ann., 137, 177 (1869), as cited in E. Schmid and I.W. Boas, Plasticity of Crystals, p. 169, p. 241, Chapman and Hall, London, 1950.

77. K.N. Subramanian and J. Washburn, "Fatigue Deformation of Magnesium Oxide," J. Appl. Physics, 34, 3394 (1963).

78. K.N. Subramanian, "Work Hardening and Deformation Structure in Lithium Fluoride Single Crystals," Ph.D Thesis, Michigan State University, East Lansing, MI, 1966.

79. K.N. Subramanian, "Cyclic Stressing in Crystals of Rock-Salt Structure," Phys. Stat. Sol., 28, 9 (1968).

80. J.D. Eshelby, F.C. Frank, and F.R.N. Nabarro, "The Equilibrium of Linear Arrays of Dislocations," Phil. Mag., 42, 351 (1951).

81. R.J. Stokes, T.L. Johnston, and C.H. Li, "The Relationship between Plastic Flow and the Fracture Mechanism in Magnesium Oxide Single Crystals," Phil. Mag., 4, 920 (1959).

82. K. Tanaka, Y. Kitahara, Y. Ichinose, and T. Iimura, "Fracture Analysis of Single Crystal Maganese Zinc Ferrites Using Indentation Flaws," Acta Metall., 32, 1719 (1984).